Calibration of Photomultipliers of the MEG LXe Detector

Xue Bai

Feb 2009

Abstract

The MEG experiment aims at discovering the lepton flavor violating decay of muon. One of the most important devices in MEG experiment is liquid xenon γ-ray detector. Equipped with 846 PMTs submerged in 880 liters of liquid xenon, it provides a precise way to detect the γ-rays produced from decay. The key to find such lepton flavor violating process with a branching ratio up to 10^{-13} , is a full understanding and improvement of the detector performance. Through various ways such as radiative decay, $\pi 0$ decay, alpha, LED etc., we calibrate the xenon detector to better understand its sensitivity and find ways of improvement. One of the significant tasks is the measurement of quantum efficiency, which is not only an important monitor of PMT performance, but also an indispensable tool for other calibrations. A precise measurement will lead to the enhancement of detector sensitivity. The current accuracy is around 2.8%. The uncertainty of such measurement is mainly due to inconsistency with simulation, i.e., our lack of knowledge of the properties of liquid xenon. After comparing data with results of simulation, it was concluded that the Rayleigh scattering length might be much longer than originally thought, at close to 85cm.

Contents

Introduction

One of the greatest success of the twentieth century physics is the establishment of the Standard Model, which explains the interactions of fundamental particles and has successfully predicted the outcome of a large variety of experiments that have been carried out. However, there are limitations to it and physicists around the world are motivated to search for new physics beyond the Standard Model.

One effective method for such a challenging quest lies within Lepton Flavor Violation. The MEG experiment aims at discovering a lepton-flavor-violating decay with a sensitivity of 10^{-13}. Recent theoretical studies on theories such as SUSY-GUT suggest that occurs with a decay branching ratio around 10^{-14}. Therefore there is a good chance of discovery with MEG.

To make a discovery of such a rare reaction, we need detectors with extremely high sensitivity. One of the most important devices in this experiment is liquid xenon detector for detecting gamma rays. Comprised with 846 photomultiplier tubes (PMTs) submerged in 800l liquid xenon, it is a novel detector and provides a high sensitivity. Operating PMTs in such an environment is difficult and challenging, and studies on performances of PMTs in liquid xenon are of great importance. One of the properties of PMTs is quantum efficiency (QE) and an accurate measurement is needed in order to better understand the detector and to improve its performance.

In this thesis, calibrations of liquid xenon detector, in particular, measurement of QE and its accuracy is discussed. In Chapter 1, the physics motivation of the MEG experiment is discussed and an overview of the MEG experiment is described in Chapter 2. Chapter 3 explains the method of PMT calibration, in particular, how to measure QE and its significance to the experiment, while the details of improving QE measurement are discussed in Chapter 4. The conclusion is written in Chapter 5.

Chapter 1

Physics Motivation

1.1 Lepton Flavor Violation

In the minimal Standard Model, neutrinos are assumed to be in one helicity state and hence considered to be massless. This assumption causes the conservation of lepton flavor. So all lepton flavor violating processes, such as $\mu \to e\gamma$ and $\tau \to \mu\gamma$, are strictly forbidden.

With the introduction of neutrino mass, lepton flavor violating process can occur at a unmeasurably small branching ratio ($\mathrm{O}(10^{-40})$). However, in theories such as SUSY-GUT, LFV is predicted to be at a measurable level that is quite close to the current experimental limit. Therefore LFV process such as $\mu^+ \to e^+\gamma$ is a promising method to testify theories like SUSY-GUT and a gateway to new physics beyond the Standard Model.

1.2 Supersymmetry and Standard Model

In Standard Model, the interaction between fermions are mediated by gauge bosons $W^\pm$, Z^0 and electroweak sector, and the interaction between quarks are mediated by gluons of the strong sector. The electroweak sector is described by $SU(2) \otimes U(1)$ symmetry, while the strong sector is described by $SU(3)$ color symmetry. Such framework has been in great agreement with experiment. However, when one attempts to unify the electroweak and strong interactions at high unification energy ($E_{GUT} \sim 10^{16}$), difficulties arise, which is called the hierarchy problem. Assuming that Higgs mass is around electroweak scale, there would have to be an incredible fine-tuning cancellation between the quadratic radiative corrections and the bare mass for the Standard Model to apply at GUT scale.

An elegant solution of the hierarchy problem is the introduction of supersymmetry, which is a symmetry that relates fermions and bosons. A generator of supersymmetry is an operator which transforms a bosonic state into a fermionic state, and vice versa. The simplest way of incorporating supersymmetry into Standard Model (Minimal Supersymmetric Standard Model) introduces one particle that differs by half a unit of spin to each existing fundamental particle. These pairs, or supermultiplets, consist of both fermionic and bosonic states, which are

known as superpartners of each other. Supersymmetry reduces the size of the quantum corrections of Higgs mass by having automatic cancellations between fermionic and bosonic Higgs interactions and thus solve the hierarchy problem.

With regards to $\mu \to e\gamma$, the introduction of supersymmetry enhances the branching ratio significantly by bringing additional sources of flavor mixing from sleptons. The branching ratio predicted by either of the following models is reachable by experiments.

1.2.1 SU(5) Supersymmetric Grand Unified Theory

In order to unify strong interaction and electroweak interaction, a single group that embeds both$SU(2) \otimes U(1)$ electroweak symmetry and $SU(3)$ color symmetry. The simplest of such groups is $SU(5)$ which is spontaneously broken at very high energy scales. In $SU(5)$SUSY-GUT, leptons are quarks belong to the same multiplets and slepton mixing at GUT scale occurs naturally. The LFV process, $\mu^+ \to e^+\gamma$, is thus enhanced through loop diagrams shown in Fig.1-1. $SU(5)$SUSY-GUT only allows LFV through right-handed sleptons. The predicted branching ratio is shown in Fig 1-2.
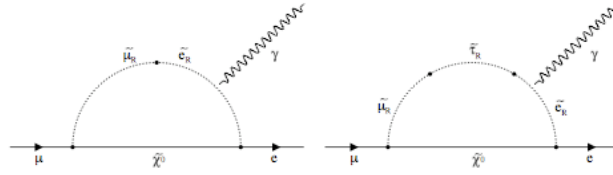
Figure 1.1: Feynman diagrams of $\mu^+ \to e^+\gamma$ in SU(5)SUSY-GUT
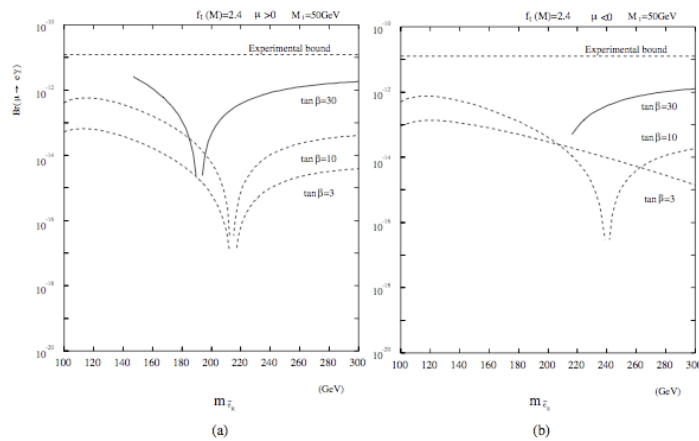
Figure 1.2: Predicted branching ratio of $\mu^+ \to e^+\gamma$ in SU(5)SUSY-GUT

4

1.2.2 MSSM with Right-Handed Neutrino

To explain to small mass of neutrinos, the seesaw mechanism introduces a heavy right-handed neutrino into the Standard Model, which also relates to LFV process. The branching ratio in this scenario depends on the Majoron mass of the right-handed neutrino. In fig1-3, the branching ratio of $\mu^+ \to e^+\gamma$ in MSSR with right-handed neutrino in the case of MSW large angle solution, a possible solution to solar neutrino mixing.
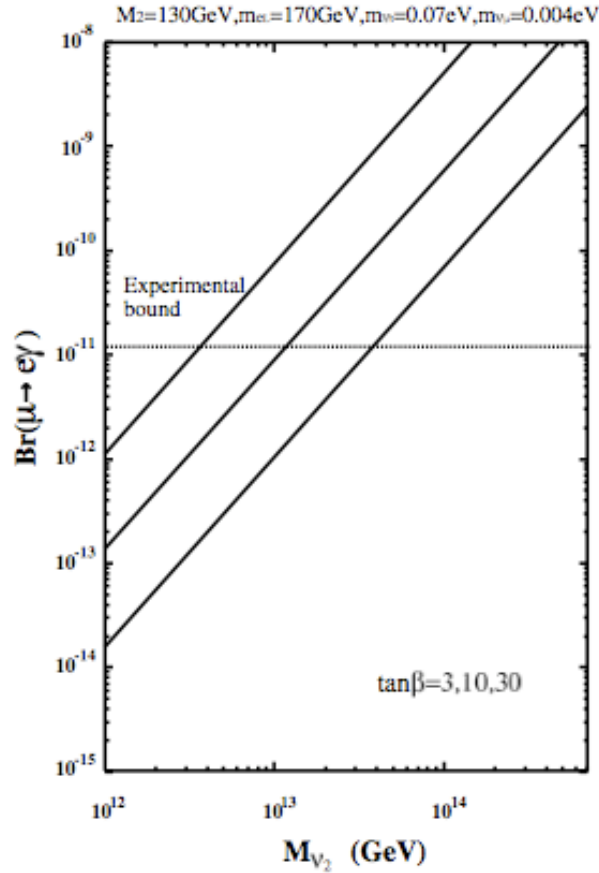
Figure 1.3: Branching ratio of $\mu^+ \to e^+\gamma$ according to MSSMRN in the case of MSW large angle solution. The three lines represent where $tan\beta = 30.10, 3$ respectively.

1.3 $\mu \to e\gamma$ search experiments

As discussed above, $\mu^+ \to e^+\gamma$ decay is a way to examine many interesting theories beyond the SM in physics such as super-symmetry and its breaking mechanism, GUT theory and the origin of neutrino mass. Thus many experiments have been conducted so far. The major experiments are listed below.

The current limit is set by MEGA.

Year	Experiment	Site	Upper Limit	Reference
1977		SIN(presently PSI)	1.0×10^{-9}	[6,7]
1977	TRIUMF		3.6×10^{-9}	[8]
1979		LANL	$1.7|times10^{-10}$	[9,10]
1986	Crystal Box	LANL	4.9×10^{-11}	[11]
1999	MEGA	LANL	1.2×10^{-11}	[5]

Table 1.1: Branching ratio of major $\mu^+ \to e^+\gamma$ experiments in the past years

Chapter 2

The MEG Experiment

The MEG experiment takes place at Paul Scherrer Institut (PSI) in Switzerland. In order to reduce background events, precise measurement of energy, emission angle and time of positron and gamma are very important.
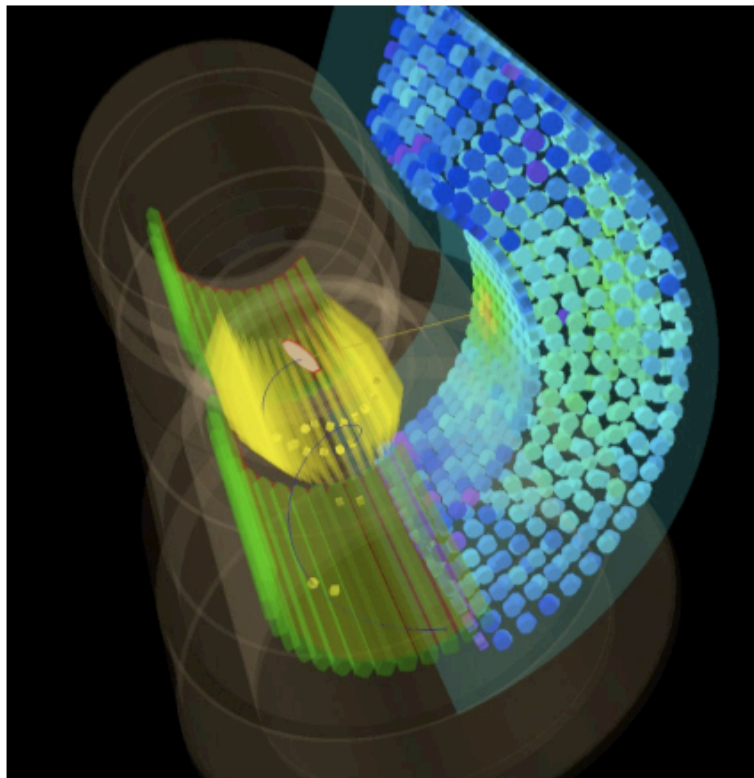
Figure 2.1: An event display during MEG physics run. Reconstructed hits and tracks are shown.

The detectors of MEG consist of positron detector and gamma-ray detector, for the detection of the two products of $\mu^+ \to e^+\gamma$, respectively. The cut view of the detectors is shown in Figure 2.2.
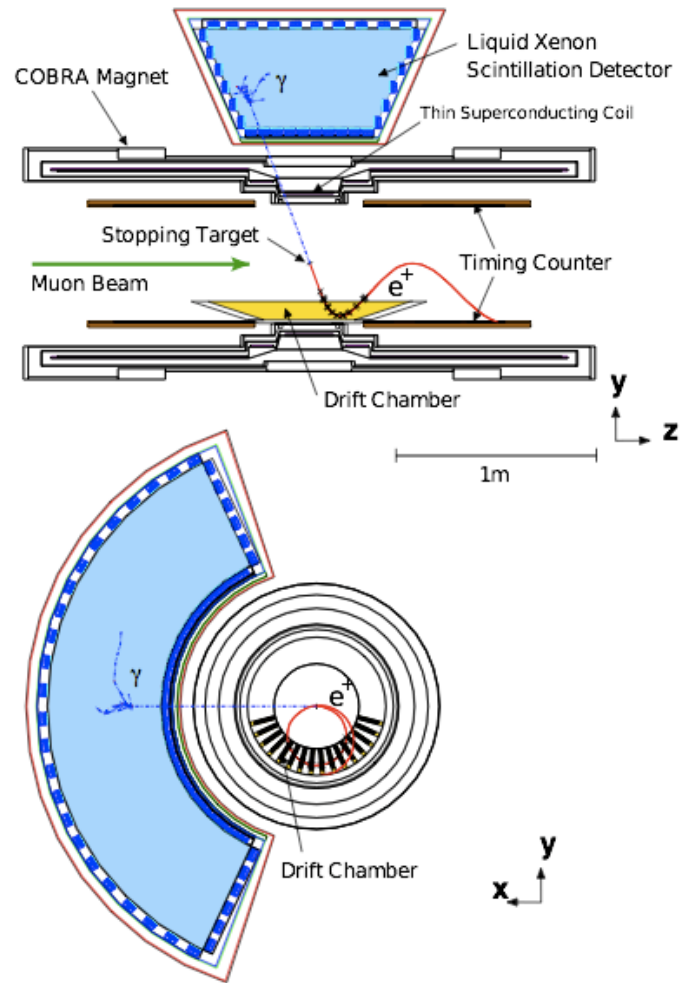
Figure 2.2: Schematic view of MEG detectors

2.1 Beam and Target

For muon beam, the πE5 beam line at PSI, the most intense DC beam in the world with an intensity of $2 \times 10^8 \mu^+/$s is used. A surface muon beam is produced from pion decays on the surface of the production target.

Muons are transported to the stopping target through Triplet I (quadrupole triplet), a Wien filter, Triplet II (quadrupole triplet) and a beam transport solenoid(BTS). The target is a polyethylene/polyester sandwich foil supported by a Rohacell frame. The target is in an ellipse shape (Figure 2.3) and put at a slant angle of 20.5° in the middle of the COBRA magnet, as shown in Figure 2.4.

Figure 2.3: A picture of the stopping target.

2.2 Positron Spectrometer

The positron spectrometer consists of a magnet specially designed to form a gradient field, a drift chamber system to measure the positron momentum and scintillation counters to measure the positron timing.

2.2.1 COBRA Magnet

A COBRA (COnstant Bending RAdius) magnet is used to produce a gradient field. Compared with a simple uniform solenoidal field, it has the following advantages:

- Positrons are swept away much more quickly, which contributes to the minimization of backgrounds.

- The positrons follow trajectories with a constant projected bending radius independent of the emission angle. This allows us to define the absolute momentum window of positrons to be detected.
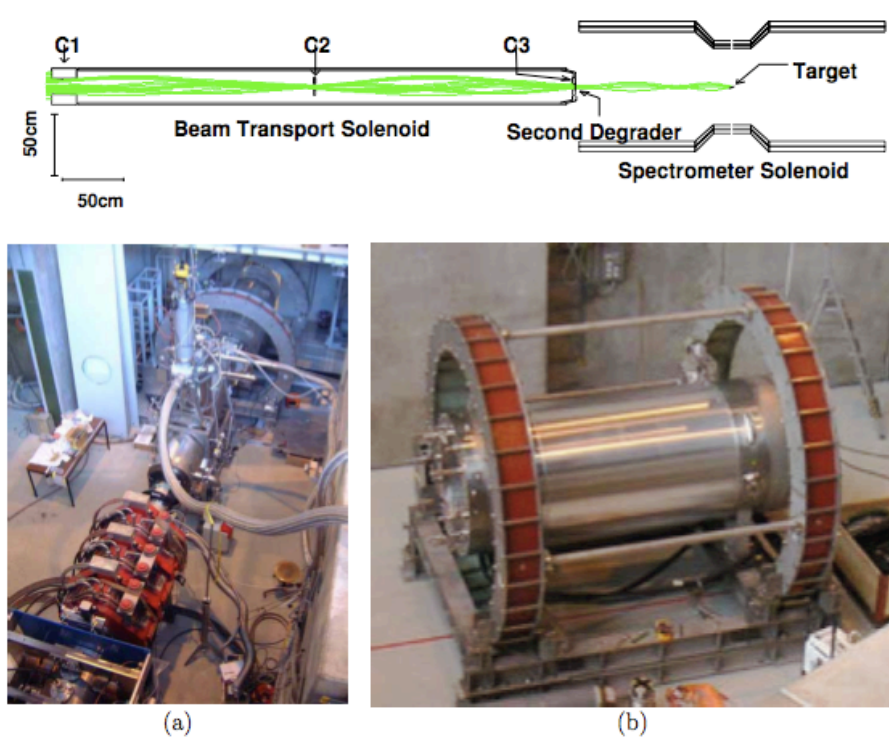
Figure 2.4: (a)Muon beam carried to target inside the COBRA magnet by the Beam Transport Solenoid (BTS). (b)COBRA magnet.
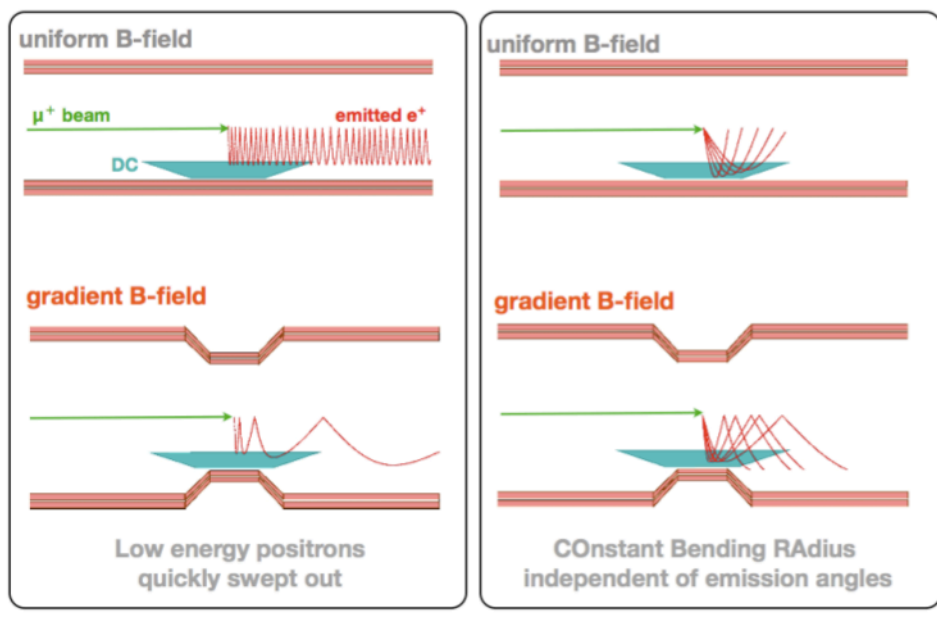
Figure 2.5: Comparison between uniform and gradient magnetic field.

2.2.2 Drift Chamber

Positron tracks are measured by a drift chamber system consisted of 16 chamber sectors aligned radially at 10 intervals in azimuthal angle. Each sector is made up from 2 staggered arrays of drift cells which measure the time and r-coordinate of positrons simultaneously. The chamber walls are made of thin plastic foils. A thin layer of aluminum deposit on the four cathode foils is shaped to make a Vernier pattern. By comparison of the charges induced on the two sets of Vernier pads of each cell, it is possible to determine the z position with an accuracy of about 300μm.

The chamber sectors and the volumes between them are filled with 50%He 50%C_2H_6 gas mixture at 1 atm, in order to minimize multiple Coulomb scattering of tracks.
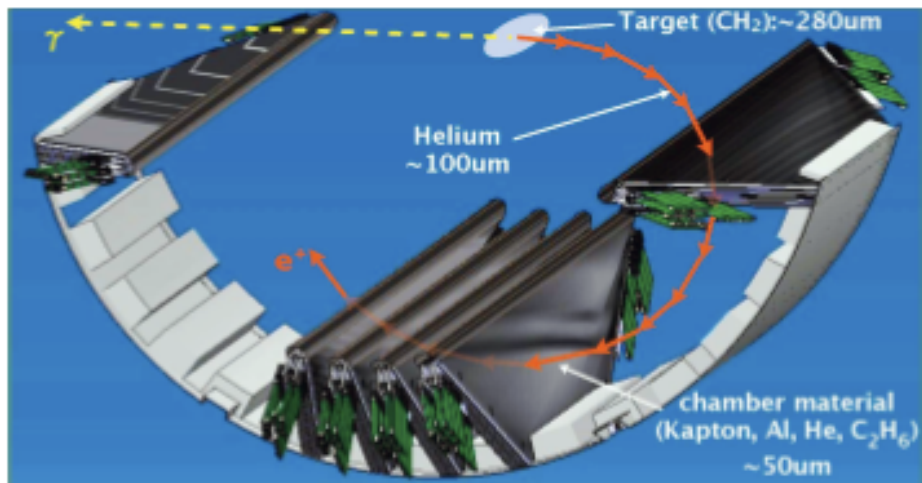
Figure 2.6: Schematic view of the drift chamber system.
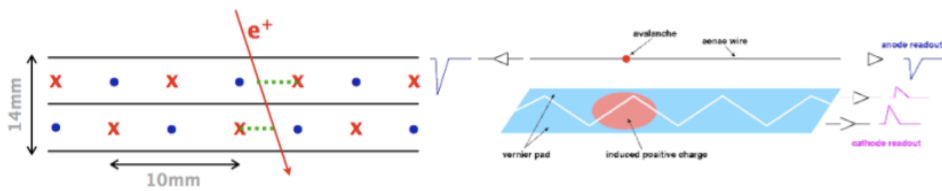
Figure 2.7: Cross view of the drift chamber and reading from Vernier pads.

2.2.3 Timing Counter

The positron timing is measured by timing counter, which consists of two arrays of scintillation hodoscopes (composed of $\sim$ 5cm wide scintillator bars) orthogonally placed along the ϕ and z directions, respectively. The outer layer will be used for timing measurement while the inner one will serve mainly for triggering purposes.

ϕ counters are straight plastic scintillatior bars lying along z direction as shown in Figure 2.8. Two inch fine-mesh PMTs are attached to both ends. While a z counter is a curved scintillation fiber put perpendicular to ϕ counters as shown in Figure 2.9. The timing resolution is expected to be 100ps FWHM.
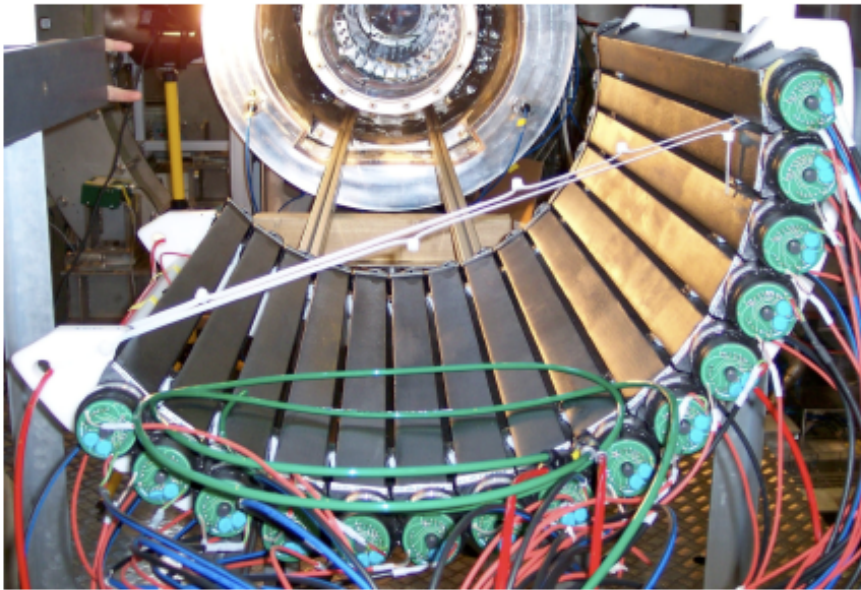
Figure 2.8: A picture of timing counters (ϕ-measuring counters).
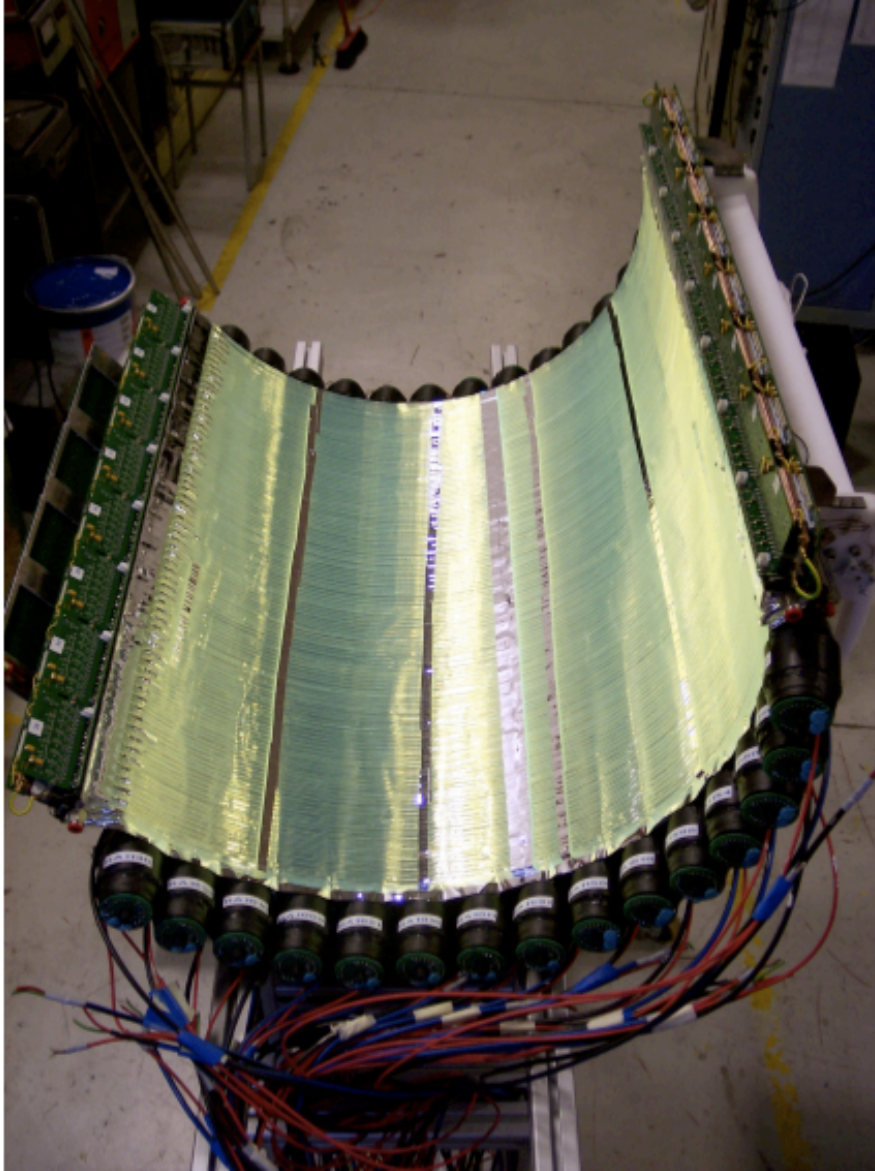
Figure 2.9: A picture of timing counters (z-measuring counters). 256 curved scintillators are put on top of ϕ-measuring counters. Also seen are the attached readout cards.

2.3 Liquid Xenon Detector

The gamma ray detector for the MEG experiment is a liquid xenon scintillation detector that is a 0.8 m^3 volume of liquid Xe viewed by arrays of 846 photo-multipliers (PMTs) from all side. A schematic view of the detector is shown in Figure 2.10. Definition of six faces of the PMT holders (inner, outer, upstream, downstream, top, bottom) are shown in the figure. The PMTs are immersed in the liquid xenon to observe scintillation light directly. Gamma rays from the target enter the detector through an entrance window consisting of an aluminum honeycomb and carbon fiber plates. Then a gamma ray interacts with the liquid xenon and deposit energy to excite xenon molecules, resulting in emission of a large amount of scintillation light.
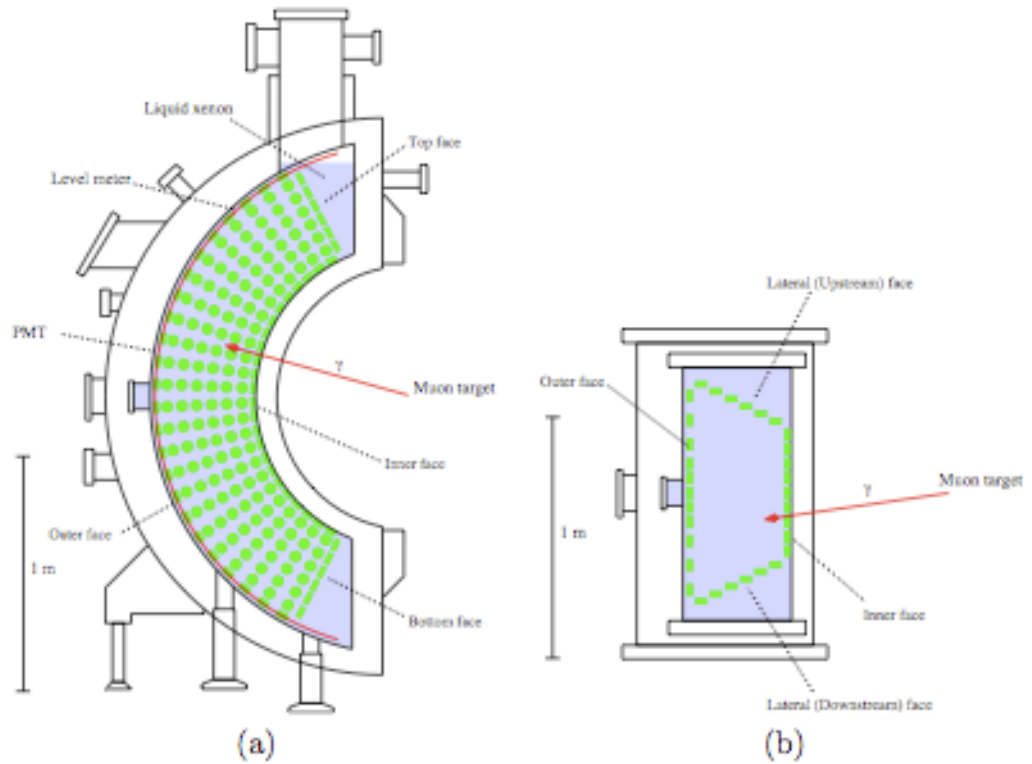
Figure 2.10: Schematic view of the MEG gamma ray detector. (a) Side view. (b) Top view.

2.3.1 Liquid Xenon Scintillator

The characteristics of liquid xenon as scintillator has been studied for a long time , but rarely has it been used in such a great volume before due to the difficulties of handling. There are many advantages of using liquid xenon as a scintillator:

- High light yield
- Fast signal
- Large proton number
- Uniformity
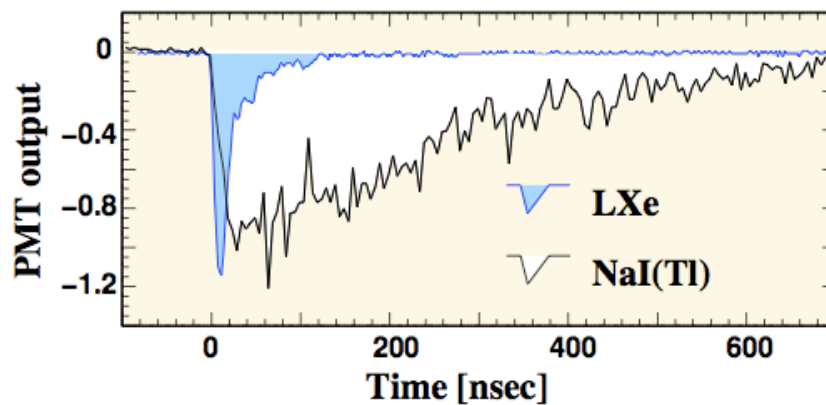
Figure 2.11: Typical waveforms of LXe and NaI(Tl) from 320keV γ rays. It is clear that liquid xenon has a much faster response compared to NaI.

These properties of liquid xenon have the benefits of :

- increasing statistics and thus enhancing resolution
- good time resolution and reduction of pile-up effects
- enablement of construction of large homogeneous detectors with a large acceptance

On the other hand, using liquid xenon also has some complications:

- vacuum ultraviolet light(VUV)
- low temperature(165K)
- high purity required
- high costs

The properties of liquid xenon are shown in Table 2.1.

15

Material Properties	Value & Unit
Atomic Number	54
Atomic Weight	131.29
Density at 161.35K	2.98g/cm^3
Boiling Point	165K
Melting Point	161K
Triple Point(temperature)	161K
Triple Point(pressure)	0.805atm
Triple Point(density)	2.96g/cm^3
Radiation Length	2.77cm
Critical Energy	10.5MeV
Mollier Radius	4.1cm
Scinti. Wavelength(peak±FWHM)	(178±14nm)
Refractive Index at 175nm	1.57 to 1.72
W_{ph} for electron	12.6eV
W_{ph} for α particles	17.9eV
Decay Time (recombination)	45ns
Decay Time (fast components)	4.2ns
Decay Time (slow components)	22ns
Absorption Length	>100cm

Table 2.1: Properties of Liquid Xenon

2.3.2 Mechanism of Scintillation Light

The origin of scintillation light from liquid xenon is de-excitation process of excited dimers of xenon, Xe_2^*. Figure 3.1 shows scintillation signals of liquid xenon by various particles. There are mainly two different processes for the de-excitation;
1.excitation process :

$$Xe + Xe^* \rightarrow Xe_2^* \rightarrow 2Xe + h\nu \qquad (2.1)$$

2. recombination process :

$$Xe^+ + Xe \rightarrow Xe_2^+ Xe_2^+ + e \rightarrow Xe^{**} + XeXe^{**} \rightarrow Xe^* \qquad (2.2)$$
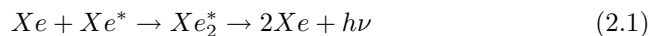
The wave length of the scintillation light emitted from both of these two processes are in the vacuum ultra-violet(VUV), 178nm(±FWHM), and the decay time constant is relatively short, 45nsec in the recombination process.
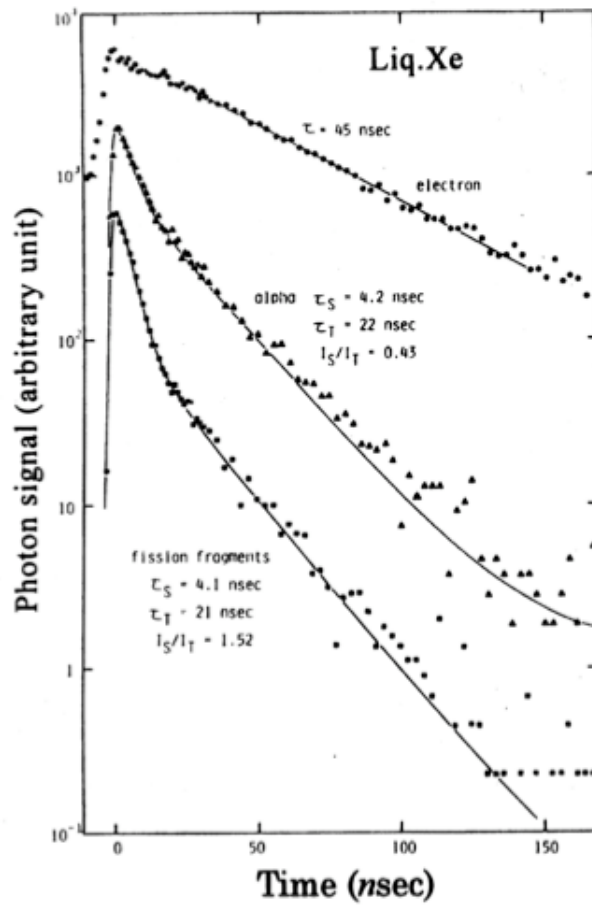
Figure 2.12: Signal of liquid xenon scintillation.

2.3.3 Photomultiplier

We cooperated with R&D Hamamatsu Photonics and developed PMT R9288. The photo-cathode material is K-ScSb. This is designed so that it can observe scintillation light of liquid xenon directly while immersed in it. To achieve that, the PMT has the following properties that are crucial to the experiment.

Detecting scintillation light from liquid xenon. A high sensitivity to VUV of 178nm wavelength thanks to the use of a quartz window that is 80% transparent to the scintillation light.

Operational in liquid xenon. Stability at low temperature of 165K.
Ability to withstand pressure up to 0.2 MPa.
Little production of impurities.

Reduction of heat load from PMT base.

Short PMT length. In order to reduce thickness of front face as well as minimize the detector volume.

Operational under magnetic field. The use of metal channel dynode structure.

Good energy resolution. Keeping of QE at low temperature.

Good timing resolution. Fast response and little time transit spread (TTS).

Figure 2.13: Hamamatsu R9288. Aluminum strips are attached on the surface of cathode to avoid increasing of surface resistance in low temperature.

The circuit diagram is shown in Figure 2. and the properties of R9288 are shown in Table 2.2 .
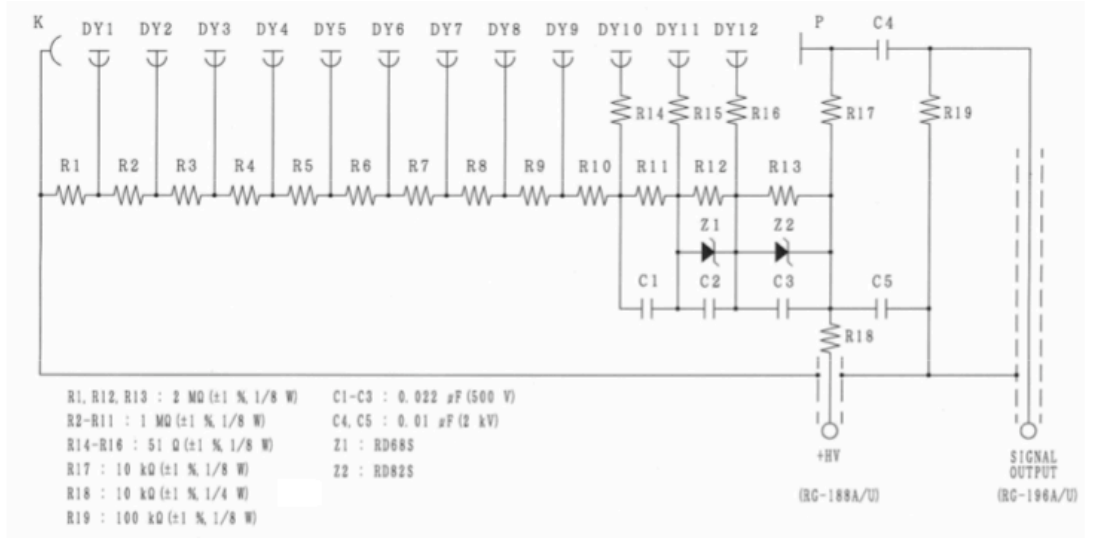
Figure 2.14: Circuit diagram of R9288.

Size	57mm ϕ
Active Area Size	45mm ϕ
PMT Length	32mm
Photocathode Material	K-Cs-Sb
Dynode Type	Metal Channel
Number of Dynodes	12
Typical HV	1000V
Typical Gain	1×10^6
Typical QE	15%
Rise Time	2.3nsec
Transit Time	16.5nsec Typ.
TTS	0.75nsec Typ.

Table 2.2: Properties of R9288

PMT Test

About 1000 PMTs were tested before installed into the liquid xenon detector. In the test, gain at 800V of HV, QE and dark current were measured. Bad PMTs (problems of base circuit, low gain or low QE) were repaired or eliminated. In Figure 2.15 , measured gain and QE of currently installed PMTs are shown. To make the response of the detector as uniform as possible, center part of the QE distribution was chosen for inner face.
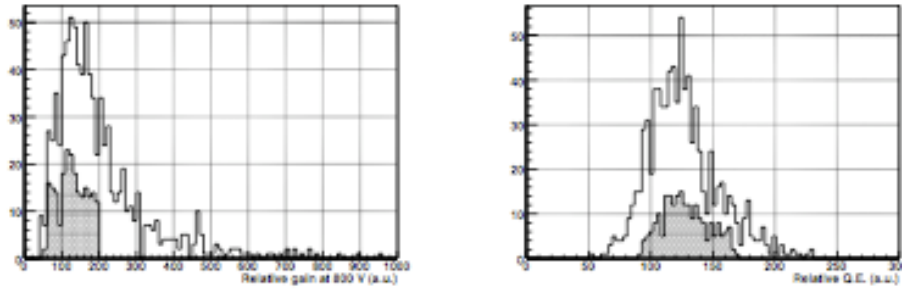
Figure 2.15: Measured gain and QE. Hatched part is PMTs used in inner face.

2.3.4   Detection Concept

Scintillation light from liquid xenon is detected by arrays of 845 PMTs located on all the walls of the calorimeter in the liquid without any transmission window. The detection principles are as following:

- The interaction position of gamma rays are determined from the light distribution observed by the PMTs.

- Energy is calculated by the light yield detected from all directions.

- The interaction time is determined by the timing information of pulses from each PMT.

The solid angle is $\Delta\Omega/4\pi \approx 9\%(0.08 < |cos\theta| < 0.35, 120\circ$ in $\phi)$. The distribution of PMTs on each surface is shown in Figure 2.18.
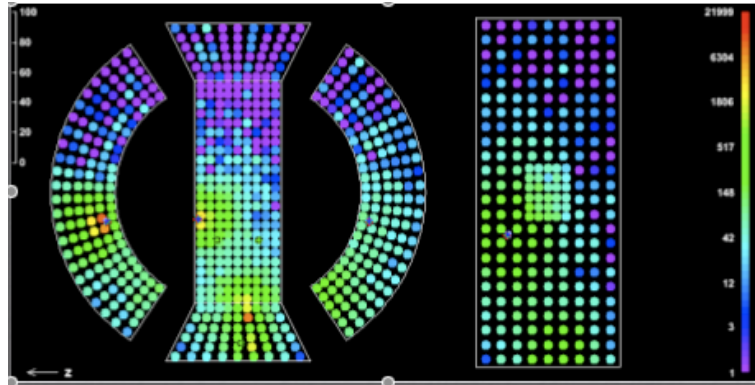
Figure 2.16: Light distribution of the PMTs.
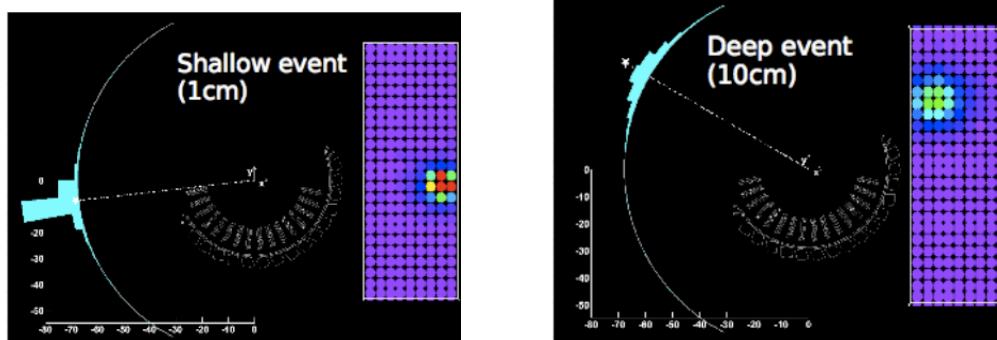
Figure 2.17: (a) Shallow event. (b) Deep event.
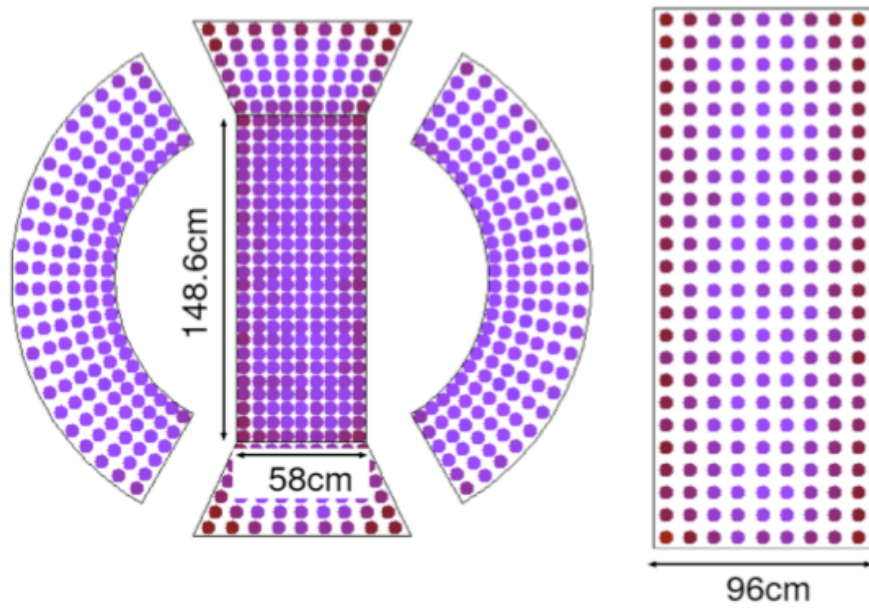
Figure 2.18: Distribution of PMTs.

2.3.5 The Xenon System

Cryostat

The cryostat is made of non-magnetic materials with low permeability. Deformation and stress of the cryostat was studied taking into account of the weight of liquid xenon. The cryostat has an inner and outer vessel. The volume between the two layers is evacuated and installed with super insulation layers.

Xenon is liquified by a pulse-tube refrigerator and a liquid nitrogen cooling pipe equipped at the top of the cryostat. The liquid xenon is kept in a stable condition by the refrigerator. Another line of LN_2 is attached on the outside of the inner vessel to directly cool the vessel. This is used mainly for pre-cooling of the vessel before starting liquefaction.

Pictures of the second LN_2 line is shown in Figure 2.19.
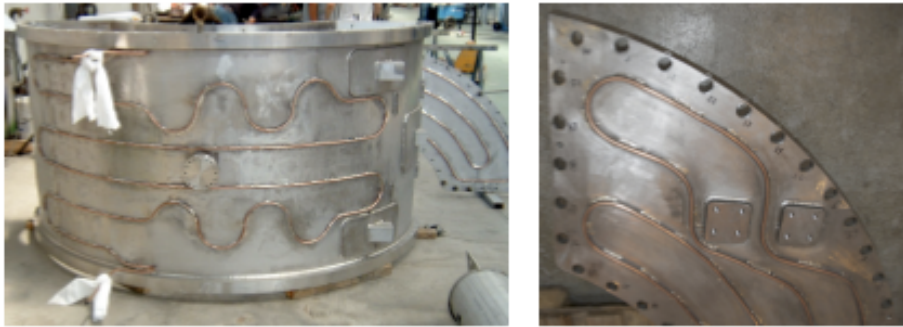
Figure 2.19: Liquid nitrogen pipe attached on inner vessel.

Handling of Xenon

The gamma ray detector for MEG uses around 1000 litters of liquid xenon and since xenon is expensive and takes time to produce, the xenon system was designed to store the xenon not in use as well. Figure 2.20 shows a schematic view of the xenon system of MEG. There are two types of storage. The GXe storage consists of eight tanks with 250 litters of volumes each. And the LXe storage (1000L storage dewar) can store about 1000 litters of liquid xenon. A purification system is installed between these two to purify GXe when it is transfered to the LXe storage tank or to the detector.

For measuring the level of the LXe, a capacitance level-meter is installed. The temperature of the xenon is measured by 27 pt-100 sensors located at various positions. Additional temperature sensors are attached on the outside of the inner vessel to monitor temperature of the cryostat. All the cables from PMTs and sensors installed in the inner vessel go to feedthroughs attached on chimneys at the top of the detector.

A heated purication getter is equipped in the purication system. The purifier removes H_2O, O_2, CO, CO_2, H_2, N_2 and hydro carbon molecules from GXe
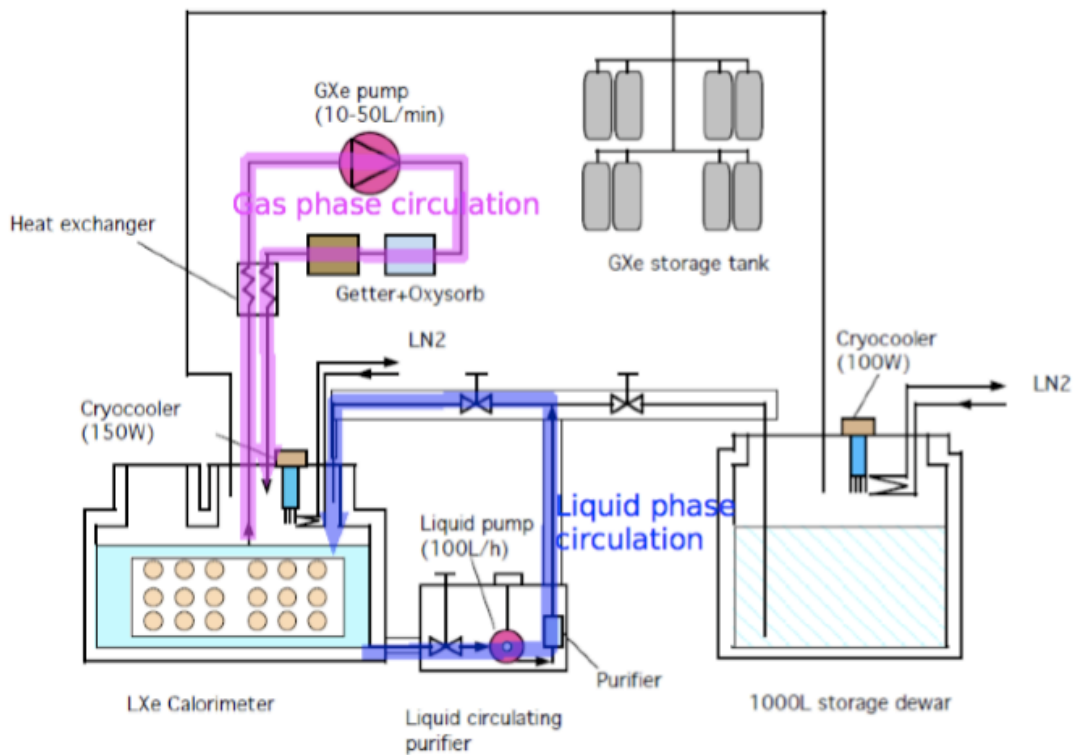
Figure 2.20: Schematic view of the xenon line.

down to 1.0 ppb. Gas purication test with 100 liters of xenon. It was confirmed that the impurities, mainly water, were successfully reduced, and an adequate performance for the MEG photon detector could be achieved. However, purification in gas phase is relatively slow, hence it is not suitable for the final gamma ray detector, which utilizes much more xenon. Therefore a purication system with circulation of xenon in liquid phase was developed. A similar system was rstly tested by using the large prototype detector. And it was found that the sys- tem reduces amount of impurities from 250 ppb to less than 40 ppb in 5 hours operation for 100 litters of xenon. Figure 2.20 is a picture of the liquid phase purifier equipped to the final detector. In the purifier vessel, centrifugal pump and purier (moleculsar sieves) are installed. The system is connected with the detector by vacuum insulated pipes to circulate xenon through the purier in liquid phase. The pump has a capability to flow xenon up to 71 liters per hour. The speed is much faster than gas purication (60 c.c. liquid per hour).

Figure 2.21: Liquid phase purification system.
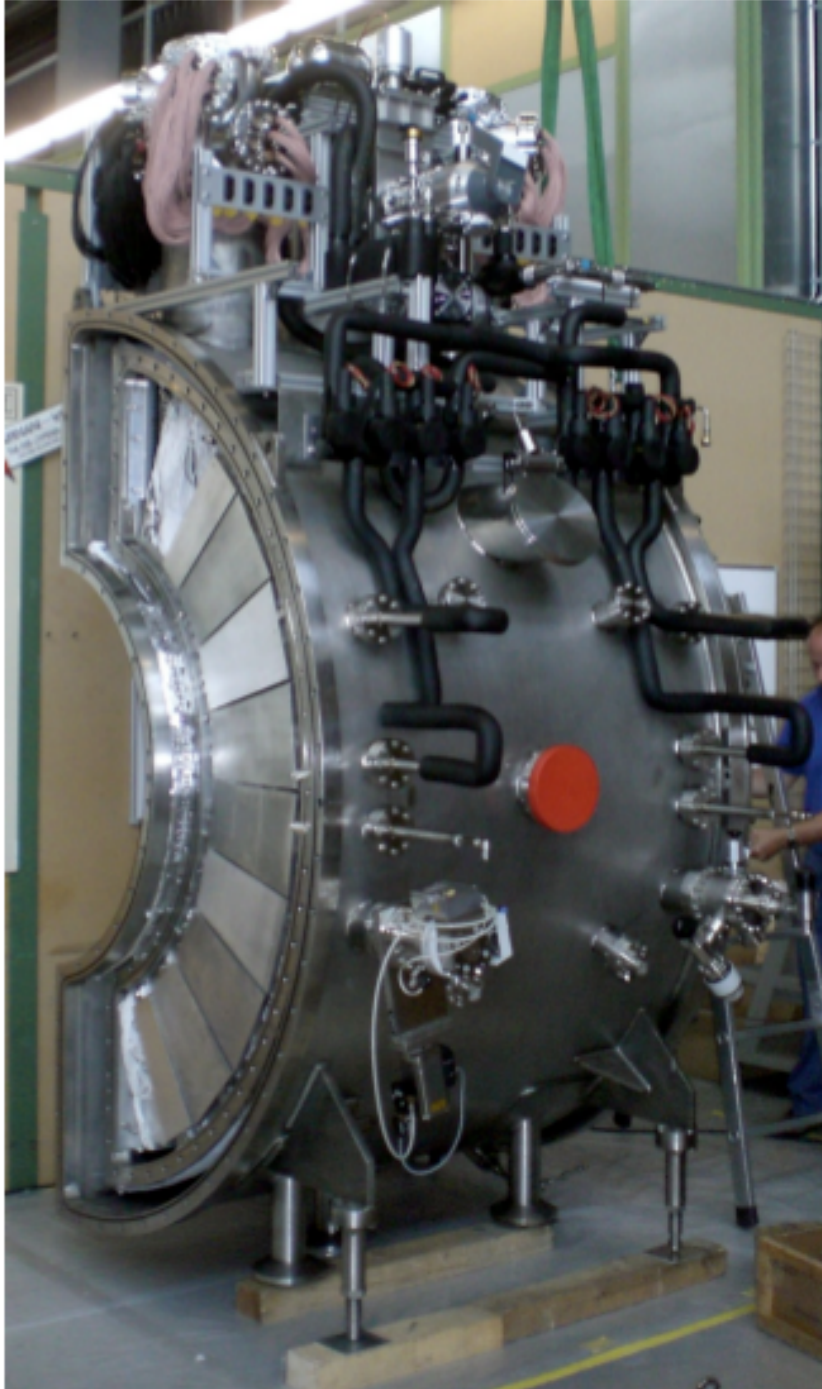
Figure 2.22: A picture of liquid xenon detector with the cryostat installed.

2.4 Background and Sensitivity

Sensitivity

The sensitivity of MEG experiment can be expressed by the following formula.

$$Br(\mu^+ \to e^+\gamma) = \frac{1}{N_\mu} \cdot T \cdot (\Omega/4\pi) \times \frac{1}{\epsilon_e \cdot \epsilon_\gamma \cdot \epsilon_{sel}} \qquad (2.3)$$

where N_μ is the stopping rate of μ; T is time of measurement; Ω is solid angle; ϵ_e is the detection efficiency of positron; ϵ_γ is the detection efficiency of gamma ray, and ϵ_{sel} is the efficiency of event selection.

The solid angle, positron and gamma detection efficiency and event selection efficiency are estimated as $0.09, 90\%, 40\%$, and 70% ,respectively.
Assuming the muon stopping rate to be

$$N_\mu = 0.35 \times 10^8/s \qquad (2.4)$$

and time of measurement to be 2 years, then the expected branching ratio is:

$Br(\mu^+ \to e^+\gamma) = 3.1 \times 10^{-14}$

These sensitivities can be converted to 90% confidence level upper limits, in case of no signal observed, by using the background rate estimates in the following section. The upper limits we obtain for the $10^8/s$ muon beam intensity is ,1.7×10^{-13}.

The estimated sensitivity of MEG detectors are shown in Table 2.3.

Gamma Energy(%)	6
Gamma Timing(nsec)	0.15
Gamma Position(mm)	9
Positron Energy(%)	0.9
Positron Timing(nsec)	0.1
Positron Position(mrad)	10.5

Table 2.3:

Background

There are mainly two types of backgrounds in $\mu^+ \to e^+\gamma$ experiment.

Prompt Background or physics background from radiative muon decays, $\mu^+ \to e^+\nu_e\overline{\nu}_\mu\gamma$.
This type of background can be identified by energy of the products. With the aforementioned resolution, prompt background can be reduced to around 3×10^{-15}.

Accidental Background with the following sources of gamma rays:

- photons from radiative muon decays
- photons from annihilation-in-flight
- photons from positron interactions with surrounding materials
- neutron induced background

The accidental background is the dominant background in MEG experiment.
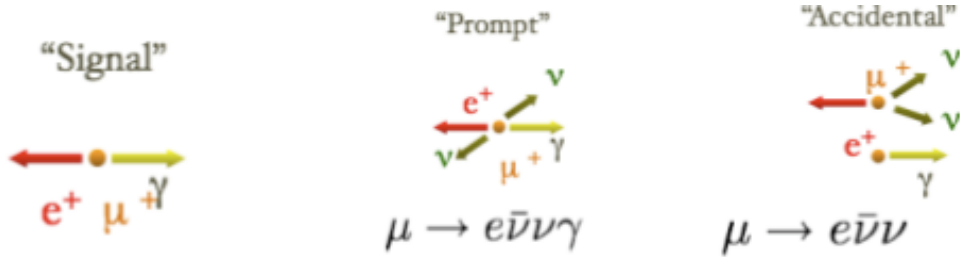
Figure 2.23: Signal and backgrounds in MEG experiment.

Figure 2.24 shows the integral yield of gamma rays, $f_\gamma(y) = \int_y^1 dy' g_\gamma(y')$. Here $y \equiv 2E_\gamma/m_\mu$ and $y = 1$ is the energy of signal. $f_\gamma(y)$ is the number of gamma rays with energy greater than $\frac{m_\mu}{2}y$ per muon decay. As shown in the plot, the energy of gamma rays in accidental background are lower than that of a signal. With an energy resolution of 2%, the background rate is 4×10^{-6} for $y > 0.98$, with annihilation-in-flight the main source.

In the case of a pile-up event, however, the energy of gamma rays may surpass that of a signal. Figure 2.25 shows the integrated pile-up yield $f_{\gamma\gamma}(y)$. With the assumed resolution values and muon stopping rate of $N_\mu = 1 \times 10^8$, the pile-up gamma rays have an occurrence rate of 1.5×10^{-6} per muon decay.
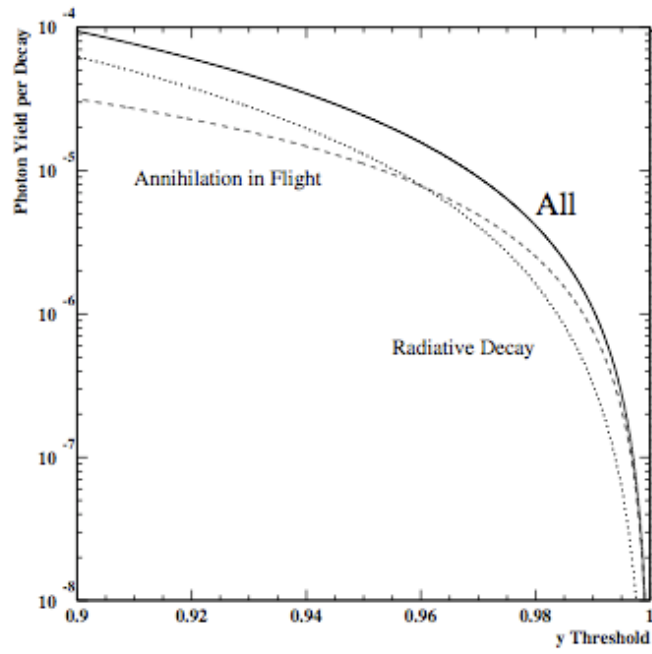
Figure 2.24: Integrated photon yield per muon decay $f_\gamma(y)$.
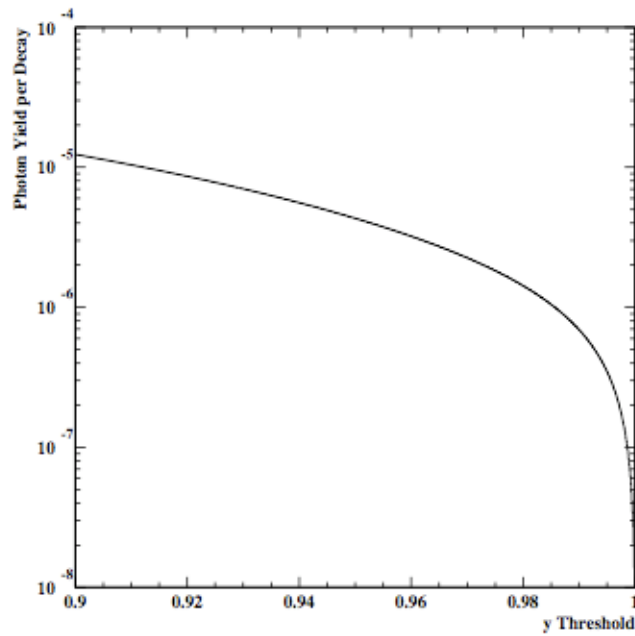
Figure 2.25: Integrated pile-up photon yield per muon decay $f_{\gamma\gamma}(y)$.

29

Chapter 3

PMT Calibration

In order to detect the signal from $\mu^+ \to e^+ + \gamma$ with a branching ratio up to 10^{-14}, high resolutions of detectors are crucial. Especially for liquid xenon detector, a precise knowledge of PMT gains and quantum efficiency (QE) is necessary for reaching an excellent energy resolution and reconstruction accuracy of the first conversion point in LXe. Hence this chapter is dedicated to the calibration of PMTs.

The LXe detector is equipped with multiple LEDs to measure gains of each PMT and ^{241}Am sources to measure QEs. Gain adjustment is for converting ADC count to the number of photoelectrons (N_{pe}) and QE values of each PMTs are necessary for converting N_{pe} to the number of photons (N_{ph}) and, in particular, for position reconstruction.

3.1 Gain Calibration

Figure 3.1: LED

3.1.1 Method

Gains of PMTs are estimated by using LEDs installed in the detector. During the measurement, several LEDs are flashed so that all the PMTs are illuminated. Data is taken by changing the intensity of LEDs. PMT gains were by using blue light LEDs which are covered with Teflon sheets with some small pinholes to attenuate emitted light so that the statistical fluctuation of LED light intensity can be small. Daily calibration was performed during data taking.

We assume that LED output is constant and the statistics of N_{pe} obeys Poisson

distribution. Some of those photons reach the quartz window of a PMT and transmit it, so that photoelectrons are generated by photoelectric effect with a certain efficiency (QE), and hit the first dynode with a collection efficiency (CE). Both obey binomial distribution. Then the photoelectrons are amplied by dynodes.

The distribution of N_{pe} becomes a convolution of binomial distributions and Poisson distribution. In that case, the upper tail is broader than lower tail. When N_{pe} is large enough (10 photoelectrons at least), the contribution of binomial distribution is negligible. Therefore the spectrum after amplication can be Poisson distribution scaled by gain. The gain can be given by the following equation:

$$g = \frac{c\sigma^2}{eM} \tag{3.1}$$

where g is the gain, c is the ADC least count (200 fC/ch), σ and M are the standard deviation and the mean of ADC spectrum tted with a Gaussian, respectively, and e is the elementary electric charge, assuming that the number of photoelectrons (Npe) observed on a PMT is so large that the ADC spectrum can be regarded as a Gaussian. In practice we have to consider a contribution from the deviation of pedestal to it as the following equation:

$$\sigma^2 = g\frac{e}{c}(M - M_0) + \sigma_0^2 \tag{3.2}$$

where M_0 and σ_0 are the mean and the standard deviation of the pedestal spectrum, respectively. The gain estimate becomes more reliable by using this equation. By changing the intensity of the LED the PMT outputs vary as shown in Fig. 3. Fig. 3. shows an example of the linear relation between σ_0 and M . The gain of the PMT is proportional to the slope of the fitting function. Thus the precision of gain determination can improve by using data for various yield of photons.
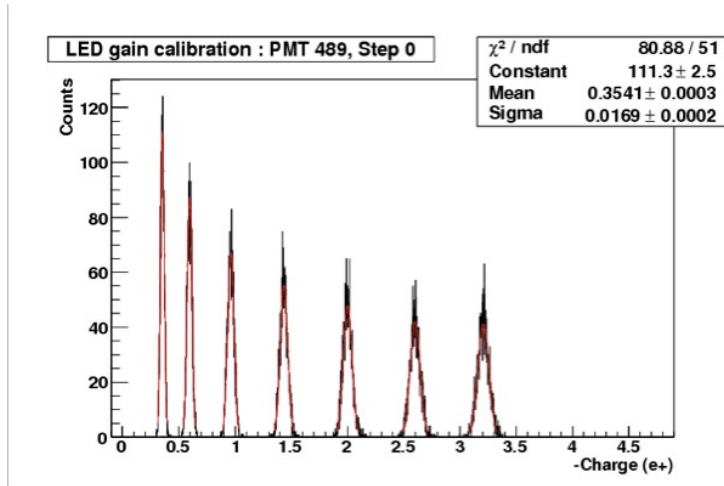
Figure 3.2: Spectrum of charge of a PMT. Intensity of LEDs are changed in 7 steps.
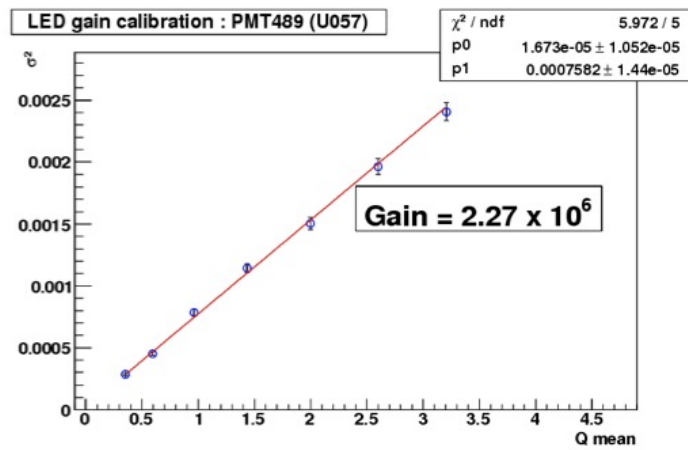
Figure 3.3: Mean and σ^2 of fitted Gaussian functions. Gain can be estimated from the slope of the plot.

3.1.2 Accuracy and Stability

The adjustment of gains, as shown previously, depend on the stability of LEDs, which is proven to be great in the long run. It was found that the gain determination can be reproduced within an accuracy of 1% in sigma and gains remain stable within 2% in the long term.
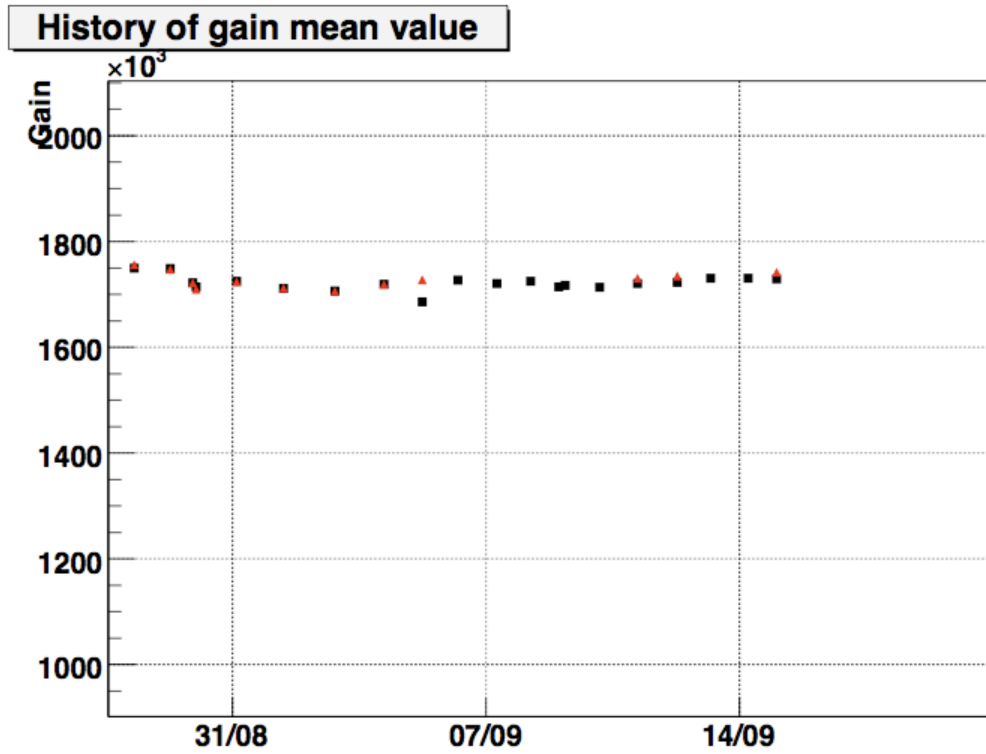
Figure 3.4: History of gain. Red and black dots represent values from trigger and DRS data respectively.

3.2 QE Measurement

3.2.1 Alpha sources

In order to measure QE, we use the same wavelength of light as Xe scintillation light since QEs highly depend on wavelength. Therefore, α particle appears to be the most reliable light source for this purpose. Alpha ray from ^{241}Am has an almost monochromatic energy spectrum (5.443MeV(83%) and 5.443MeV(15%)) with lower tail caused by energy loss in the source material itself and its range in liquid xenon is benecially short as 40μm. In addition it is very stable even at low temperature in LXe. The half life of ^{241}Am is long enough that the source intensity can be regarded as constant. Therefore the α source is a good point-like light source for estimating QEs.

Alpha sources are put on wires, each of the size 1mm. Diameter of a wire is 100μm. In total 25 alpha sources on five wires were installed as shown in Figure 3.5. A picture of an alpha source wire and LED bundle is shown in Figure 3.7.
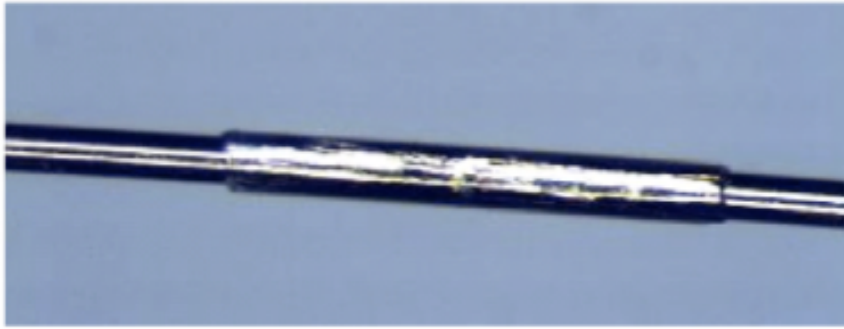
Figure 3.5: Alpha source on a wire. Length of the source is 1mm, and diameter of the wire is 100 μm.

There are three advantages of wire sources compared to plate sources:

- More scintillation light is observed by PMTs as a wire source can be seen from virtually all directions, while in the case of a plate source, half of the solid angle is covered.

- A plate source can be only put on the PMT holders, while a wire source can be put at any place without making shadows in gamma ray measurements, making it possible to illuminate all the PMTs with smaller number of alpha sources.

- Wire sources are located in the fiducial volume so the geometrical relation between PMTs and light sources is closer.
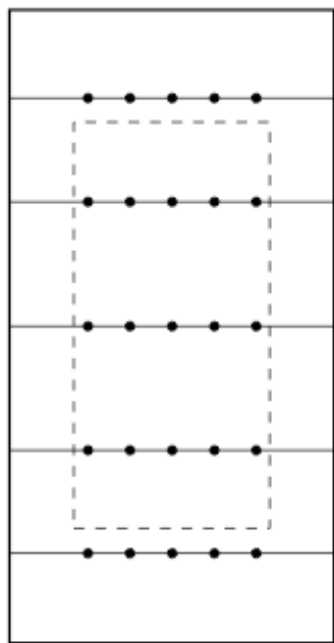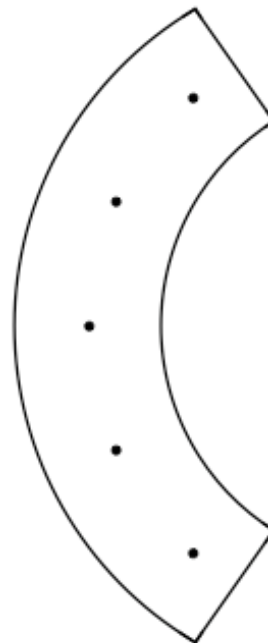
Figure 3.6: Positions of alpha sources in the detector. Solid and dashed boxes in the left figure are outer and inner faces respectively.

Figure 3.7: Alpha source wire and LED bundle.

Figure 3.8 shows the weighted mean of PMT positions in alpha events. In liquid xenon, weighted mean positions make rings shown. The range of an alpha particle is comparable to the thickness of the wire, so the wire makes shadow, as shown in Figure 3.9. The radius of the ring depends on thickness of the wire and scattering length of xenon.
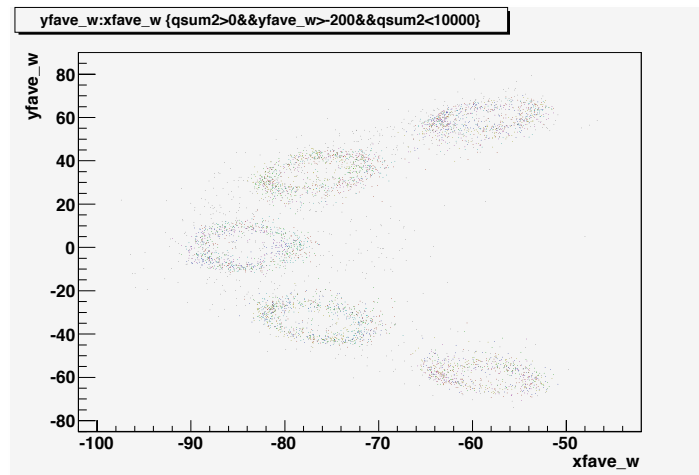
Figure 3.8: Weighted mean position of PMT outputs in alpha events in liquid xenon.
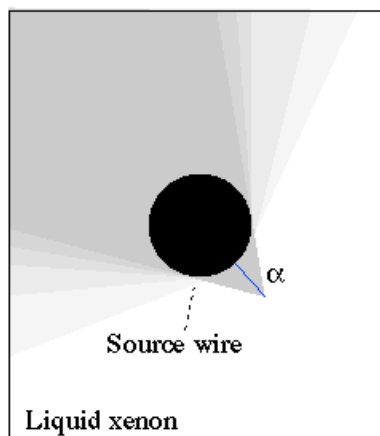
Figure 3.9: Alpha particle and the wire. Diameter of the wire is 100 μm and the range of alpha particle in liquid xenon is about 40 μm.

3.2.2 Simulation

QE is measured by comparing the charge spectra from a given alpha source with those from simulation. The outcome of such simulation depends largely on the optical properties of liquid xenon, such as absorption length, scattering length, refractive index, group velocity of scintillation light.

Rayleigh Scattering Length

Rayleigh scattering length can be estimated by comparing data observed for alpha source wires., whose reconstructed positions make rings. This is due to a shadow effect of wires as shown in Figure 3.9. A PMT observes more light for events where an alpha particle is emitted to the direction of the PMT than events where the particle is emitted behind the wire. These two cases make two peaks in the distribution of number of photoelectrons. The ratio of the two peaks is sensitive to scattering length. Using data from the large prototype, the ratio was compared with simulated data by changing scattering length in MC. The Rayleigh scattering length was estimated to be 45cm.

Absorption Length

Absorption length of scintillation light in liquid xenon has been estimated by comparing output of each PMTs for alpha source events with MC simulation as a function of the distance between the PMTs and alpha sources. Scintillation light can arrive at PMTs indirectly because of Rayleigh scattering. Therefore, the actual path length of light is not exactly same as the distance between the source and PMT, and the effective distance needs to be estimated from MC simulation by taking into account Rayleigh scattering. If we do not take into account of Rayleigh scattering effect in the simulation, the correlation between observed charges of PMTs and absorption length can de described as $e^{-d/\lambda_{abs}}$ where d is the distance between PMT and source. On the other hand in a realistic case with a finite Rayleigh scattering length, such dependence changes and thus the effective distance needs to be estimated by fitting with an exponential function with d as a free parameter. Using the effective distance estimated in this way as a distance between the PMTs and alpha sources, the absorption length was estimated in MC simulation for various cases and compared with the input values to the simulation. Before applying the method to the real data, PMT output was corrected with QE estimated with alpha data in cold gas xenon. The ratio of PMT output to MC simulation with infinite absorption length is a function of the effective distance between the source and PMTs. By fitting the distribution with an exponential function, it is found that the absorption length was 233^{+193}_{-72} during the measurement in 2003. The absorption corresponds to about 80 ppb of water contamination. In this analysis, scintillation efficiency of xenon (the W value) was assumed as 17.9 eV and 49.6 eV in liquid and gas respectively, and the scattering length was assumed as 45 cm against 175 nm ultraviolet light.

Comparing data with simulation

Figure 3.8 shows the observed charge of a PMT from a certain alpha source. To compare the data with the result of Monte Carlo, a fitting function is used. For number of photoelectrons less than 10, a simple gaussian function is used. While for more photoelectrons, we use an exponential function convolved with a Gaussian which has a spread of square root of the number of photoelectrons spread of pedestal distribution.

After fitting data with the aforementioned functions, the mean values of photoelectrons of each PMTs are compared with those of simulation and QE is estimated from the slope, as shown below.
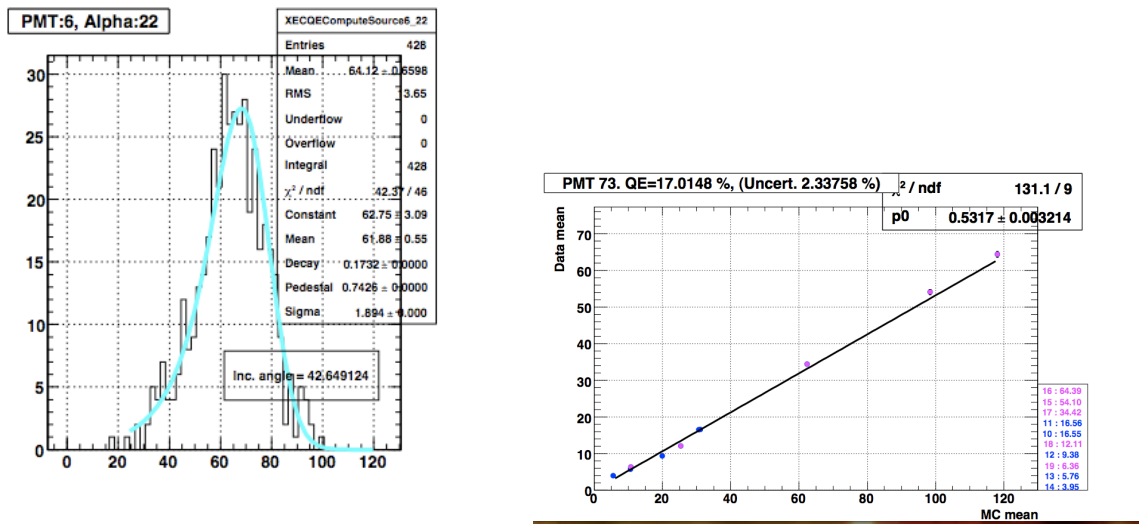
Figure 3.10: (a)An example of charge spectrum from a given alpha source observed by a PMT. (b)The mean value of the fitting function is compared with simulation. QE can be estimated from the slope.

3.2.3 Accuracy and stability

The uncertainty of QE is estimated by the error of fitting function mentioned above. The current accuracy of QE estimation is around 3%.
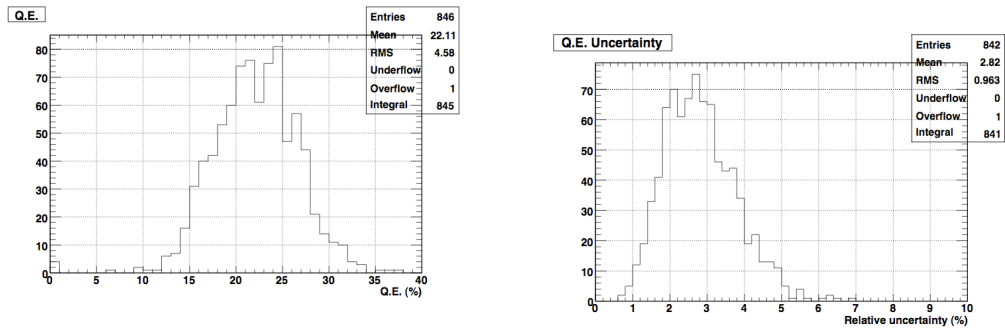
Figure 3.11: (a)Distribution of measured QE values. (b)Relative errors of QE measurement.

The long term stability is monitored and proven to be quite good. Since we always used the same gains in calculating QE, the overall equalization factor, which is the quantity of $1/(\text{gain} \times \text{QE})$, is not affected by the gain measurement at all. The uncertainty of the equalization factor is dominated by the inconsistency with MC, i.e., lack of our knowledge of the LXe property.

3.2.4 Application of QE correction

As mentioned before, a better QE measurement improves our understanding of the performance of detectors and accuracy of other calibrations as well. One example of QE correction is the application on $\pi 0$ runs. The position resolution has been significantly improved after applying QE correction.

$\pi 0$ calibration

Calibration measurements had been performed in August 2008 for about a month in order to estimate responses of the liquid xenon photon detector, especially energy, position, and timing resolutions to 55MeV gamma rays, which is close to 52.8MeV signal energy. Gamma rays from $\pi 0$ decays ($\pi 0 \to \gamma\gamma$) produced by charge exchange reaction ($\pi^- \to +p \to n + \pi^0$) were used. NaI array and plastic scintillator detector was placed opposite to the liquid xenon detector to select back-to-back photons which have almost monochromatic 55MeV, and 83MeV energy. In order to study relative timing resolution between γ ray of LXe detector and e^+ of timing counter and drift chamber, Dalitz decay events of the $\pi^0(\pi^0 \to e^+ + e^- + \gamma$, BR= 1.12%) are used. Negative pion beam introduced into the E5 area induce the charge exchange reaction in the LH$_2$ target prepared for this purpose.

Pb collimators are prepared for estimation of position reconstruction and resolution. Figure 3.12 shows the geometry and photo of Pb collimators. Left figure shows the lead collimator, whose depth is 1.8cm, with three horizontal slits of them. Right photo shows the lead collimator with three vertical slits and three horizontal slits.

These collimators were installed to four different positions in front of LXe detector as shown in Figure 3.13, and each position has two lead plates with vertical slits, or horizontal slits. Lead collimators with horizontal slits are installed to upper two locations, and those with vertical slits are installed to lower two locations. The centers of the four lead collimators are aligned to 52.3°, 0°, -15.69°, and -52.3°, respectively.

Four Pb collimators were installed just before the measurement. LXe self trigger data with 1.1M events for each Pb collimator were taken independently by using software collimator, and it took 15 hours per each position.

Event selection criteria is following. Xenon detector single trigger (#9) is selected. Depth of the first conversion point in LXe detector is more than 2cm, and energy is more than 45MeV and less than 60MeV.
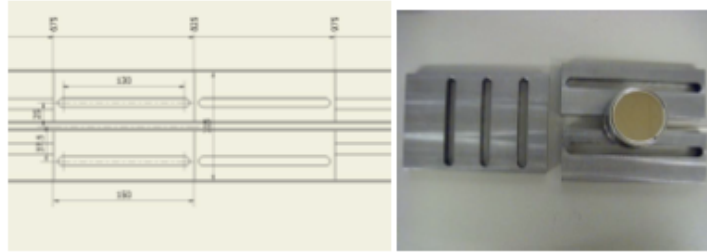
Figure 3.12: Left: geometry of Pb collimator with three horizontal slits; Right: Pb collimators with vertical and horizontal slits.
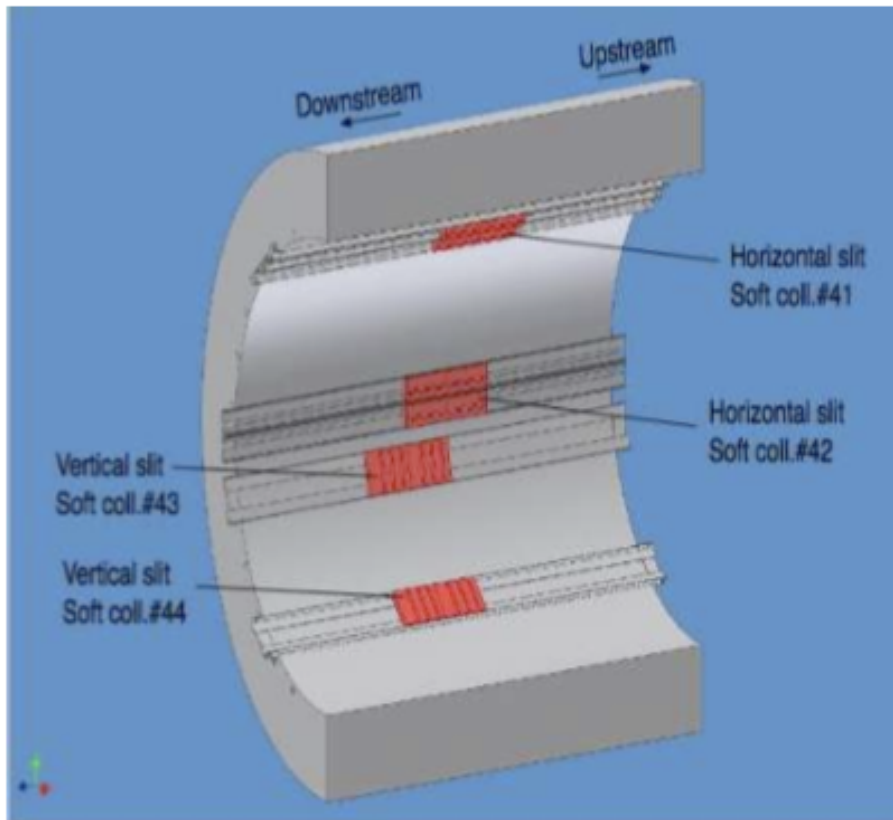
Figure 3.13: Places where Pb collimators were installed.

Figure 3.14 shows 2D reconstructed position distribution of one Pb collimator before and after applying QE correction. Horizontal axis shows u direction, and vertical axis shows v direction. The collimator has three slits at horizontal direction. Compared with the one before QE correction, the one after has a better resolution.

Figure 3.15 shows 1-D projection to the vertical axis with a horizontal vertex position slice of $|u| < 1.55$cm. We can see three peaks from the three slits and two upper and lower edges. We can get five position resolutions from this 1D histogram and two gaussian fits are shown in the figure, σs are shown as 8mm and 7.2mm, respectively.

From these figures, the position resolution is evaluated to be 4∼6mm at the edge events, and 6∼8mm at 1cm slits.
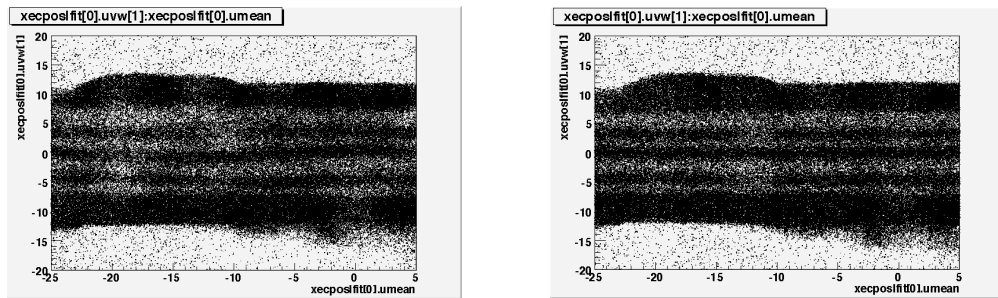
Figure 3.14: 2D vertex distribution with horizontal lead collimator before and after QE correction.
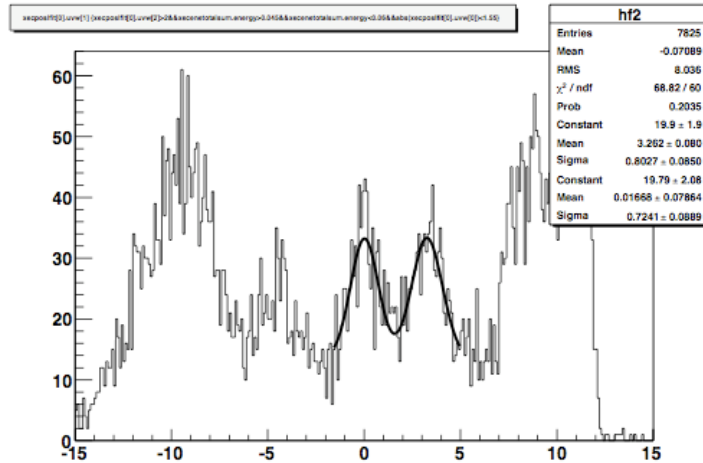
Figure 3.15: 1D vertex distribution with horizontal lead collimator.

43

Chapter 4

Study on improving accuracy of QE measurement

The current accuracy of QE estimation in LXe is 2.83% on average, which remains to be improved. The accuracy of QE measurement is determined by the error of fitting function, as shown in Figure 3.10 (b). Figure 4.1 below is and example of fitting. While ideally, all points should form a straight line, for some PMTs, there are some discrepancies between different points, i.e. differences in data and simulation.

Hence the current inaccuracy arises from the difference between simulation and data. In other words, our lack of understanding of LXe properties. By studying how to improve the accuracy of QE measurement, hopefully we will learn more about the properties of liquid xenon as well as enhance detector sensitivity.
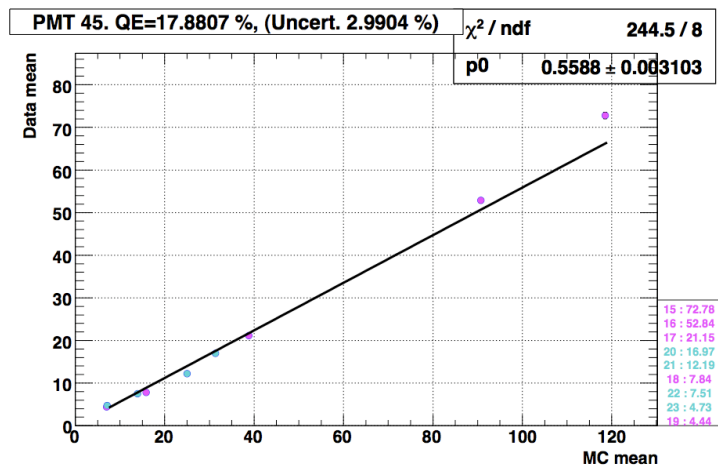
Figure 4.1: Example of QE fitting. All points are not on the same line.

4.1 Determining Factors

The current default setting in Monte Carlo is listed in table 4.1.

Parameter	Value(for λ=178nm)
Refractive index of liquid xenon	1.61
Wavelength	178nm
Rayleigh scattering length	45cm
Absorption length	∞
Reflection on PEEK	0.10
Reflection on Aluminium	0.2
Reflection on KOVAR	0.2
Refractive index of quartz	1.62
Transmittance rate of quartz	0.8

Table 4.1: Parameter setting in simulation.

Another relevant value is the cut we apply to the incidence angle. As for large angles, the scintillation light mostly come from indirect sources and can be difficult to evalue. The current cut is set as 74°Together the crucial factors in measuring QE can be summarized as:

- absorption length

- scattering length

- reflection

- incidence angle cut

The ratios between the mean values of data and MC for each PMT are plotted in relation to distance and angle, as shown in Figure 4.2 and Figure 4.3.
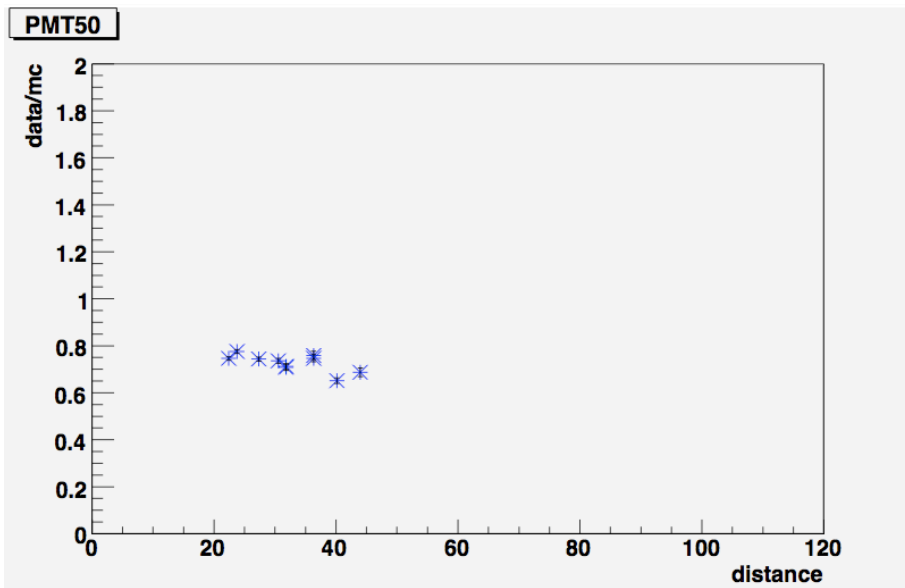
Figure 4.2: Ratio between data and simulation in relation to distance.
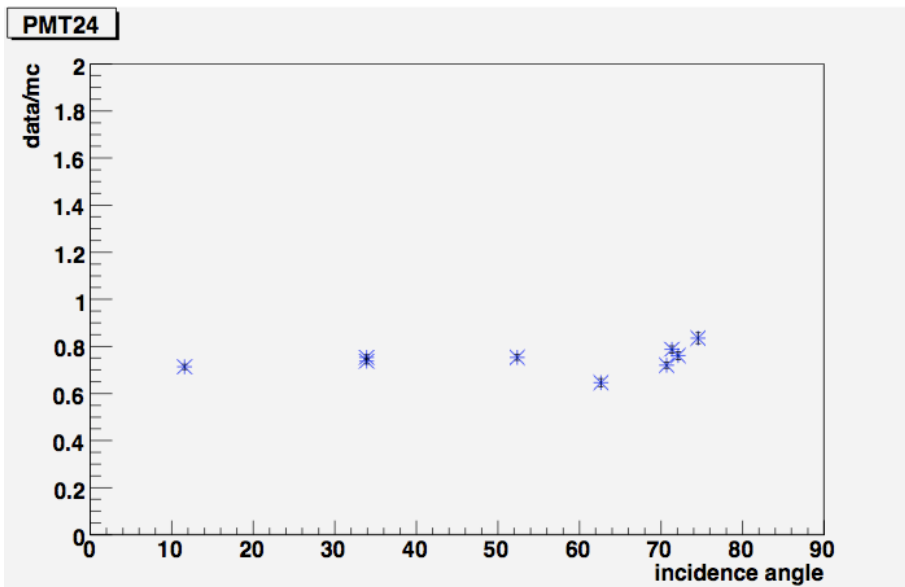
Figure 4.3: Ratio between data and simulation in relation to incidence angle.

Two traits can be observed from these plots.

- When the distance is small (< 60cm), the data/MC ratio remains relatively constant except for large incidence angles, where there appeared to be a slight drop followed by a slow climb in the ratio when angles are larger than $60°$.
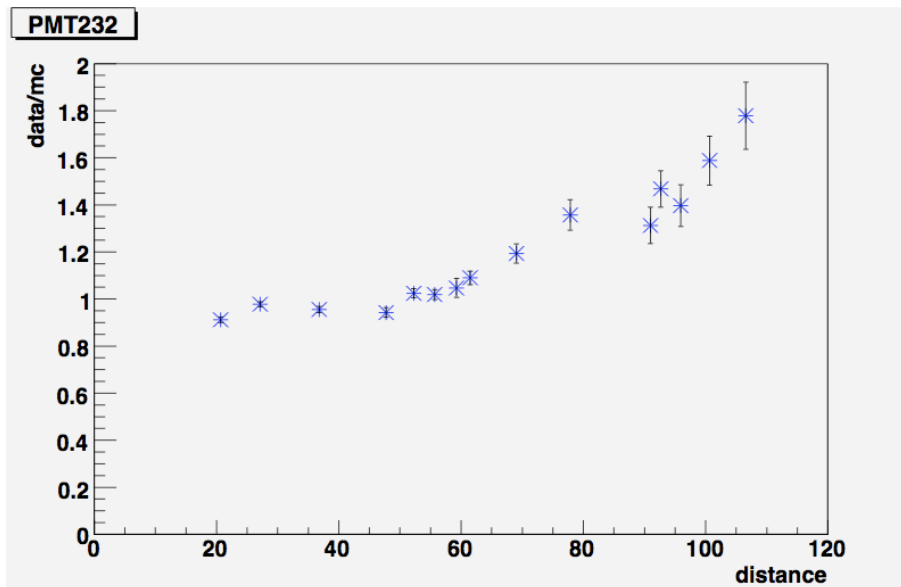
Figure 4.4:

- When the distance is large (> 60cm), the data/MC ratio increased in relation to distance drastically.

In light of these conclusions, the study was focused on the scattering length and reflection factor on various materials inside the detector. A stricter incidence angle cut was also considered. The current cut was 74°, which is quite close to the total reflection angle (around 80° assuming the refractive index of liquid xenon is 1.61).

4.2   Simulation

A set of Monte Carlo simulation was made in regard to each of these factors by increasing scattering length and turning off/increasing reflection from each material (quartz, Kovar, peek, aluminum). 50000 events were created for each setting. The comparison between these settings and the default one (MC -302) is shown in Figure 4.5. to Figure 4.10.
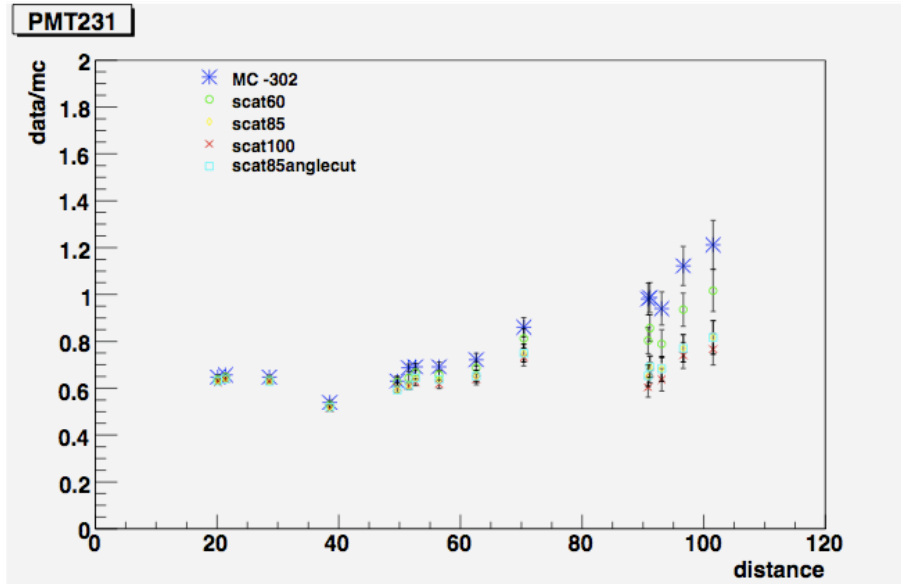
Figure 4.5: Data/MC ratio in relation to distance. Several simulations were made by changing the scattering length from 45cm to 60cm, 85cm, 100cm.
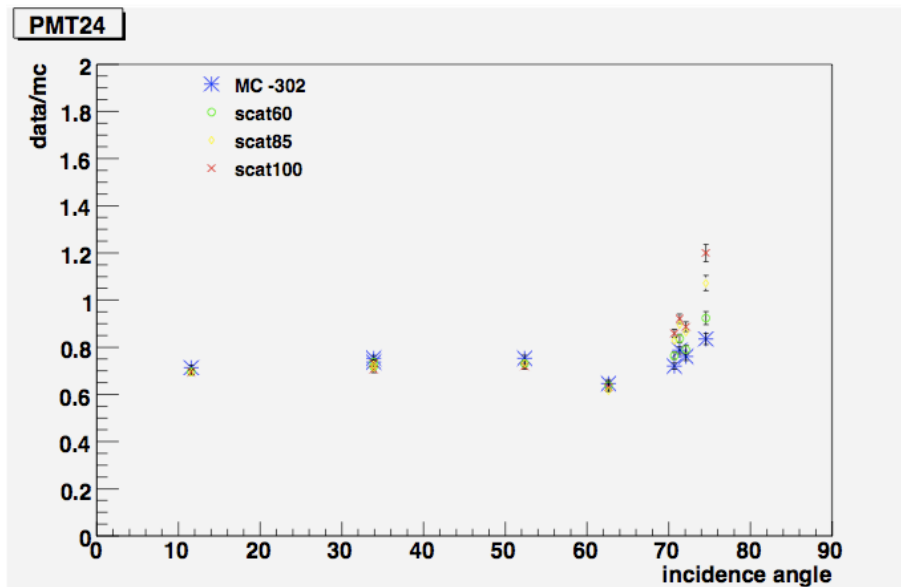
Figure 4.6: Data/MC ratio in relation to incidence angle. Several simulations were made by changing the scattering length from 45cm to 60cm, 85cm, 100cm.
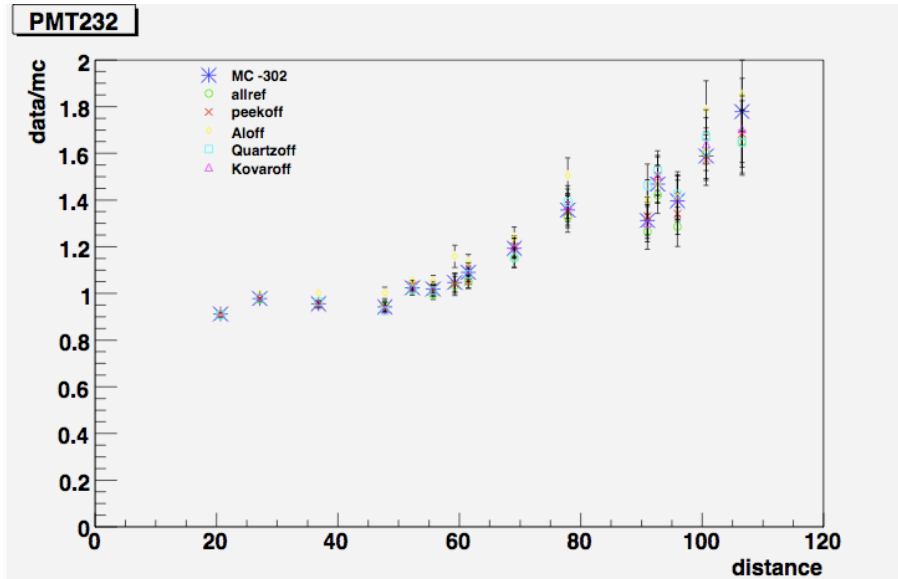
Figure 4.7: Data/MC ratio in relation to distance. Several simulations were done by turning off reflection on each material.
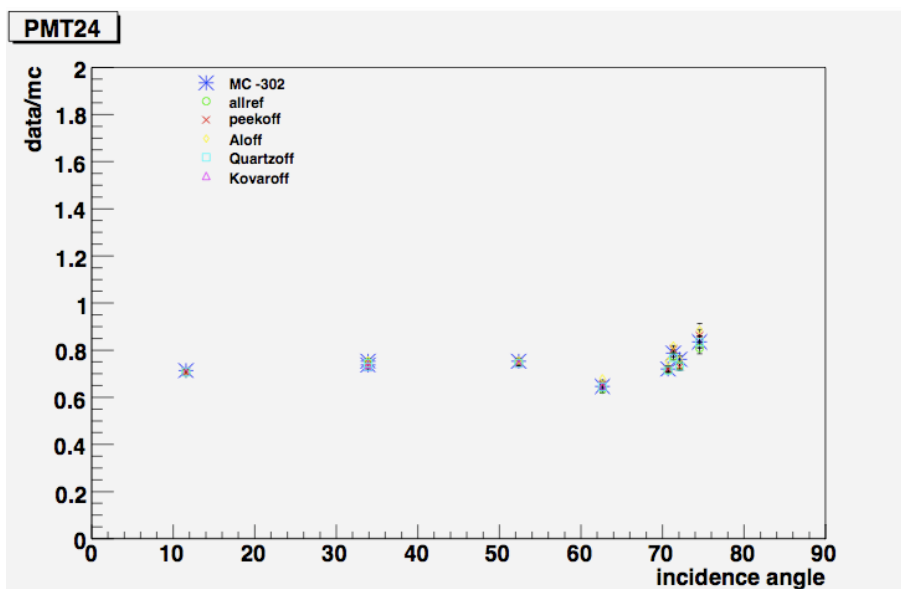
Figure 4.8: Data/MC ratio in relation to incidence angle. Several simulations were done by turning off reflection on each material.
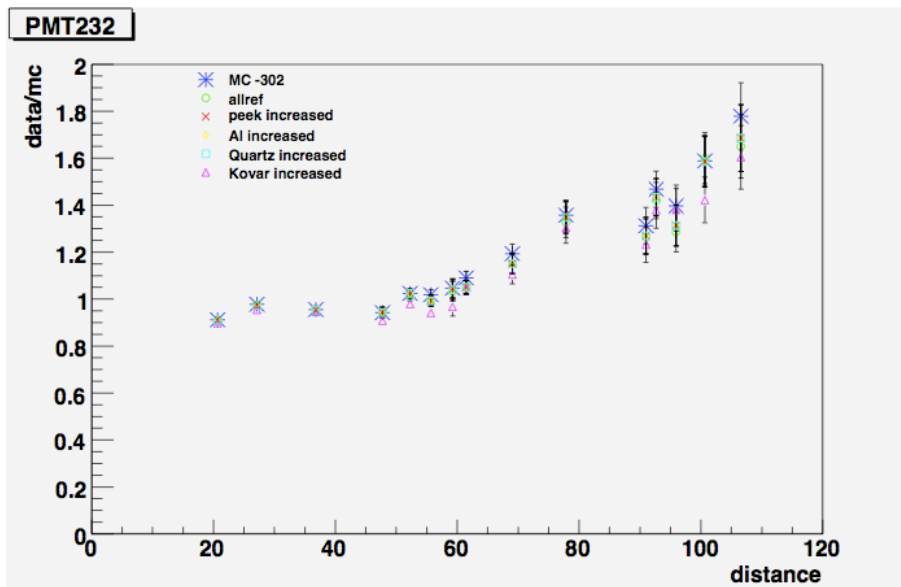
Figure 4.9: Data/MC ratio in relation to distance. Several simulations were done by increasing reflection on each material.
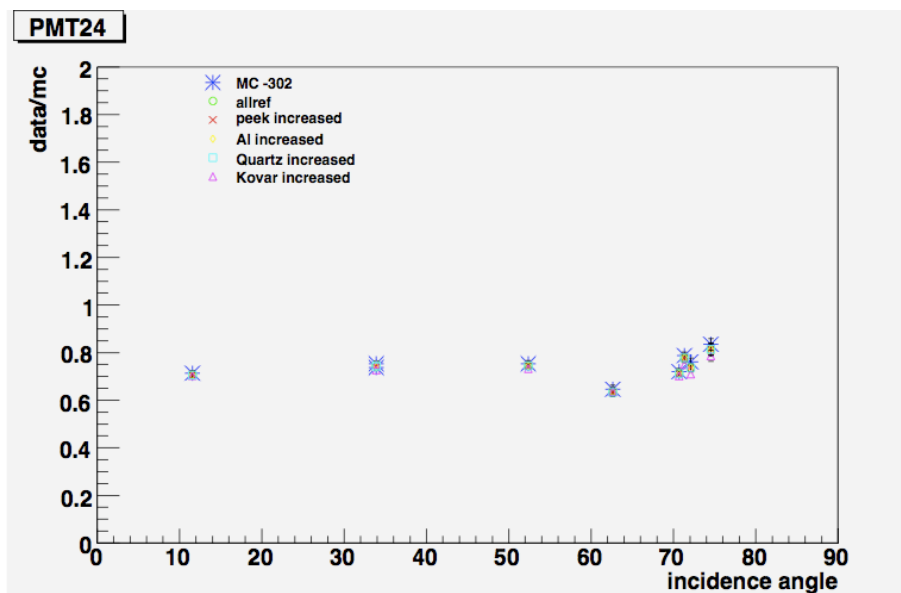
Figure 4.10: Data/MC ratio in relation to incidence angle. Several simulations were done by increasing reflection on each material.

4.3   Result

1. When scattering length was increased, the data/MC ratio in large distance dropped significantly and accuracy improved.

2. The climbing up in large angles worsened when increasing scattering length.

3. Turning off or increasing reflections on each material did not render much change in relation to distance or incidence angle.

The incidence angle was then set to 60° to make the data/MC ratio more uniform.
Judging from overall accuracy, the scattering length is believed to be close to 85cm.

Chapter 5

Conclusion

From the result mentioned in the last chapter, it can be concluded that the current most suitable setting for simulation would be for scattering length to be 85cm. Also the incidence angle cut is better reduced to 60° due to the inconsistency in large angles.

With this new setting of parameters, the uncertainty of QE measurement dropped from 2.82% to 2.32%. For PMTs in each locations (inner, outer, upstream, downstream, top, bottom), the uncertainty of QE dropped $4\%, 16\%, 26\%, 19.6\%, 36\%, 43\%$ respectively.
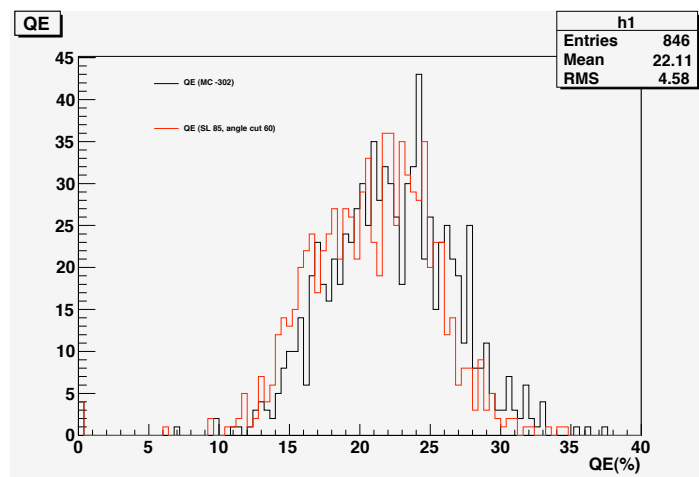
Figure 5.1: Distribution of QE with old simulation and QE with longer scattering length (85cm) and lower incidence angle cut (60◦)
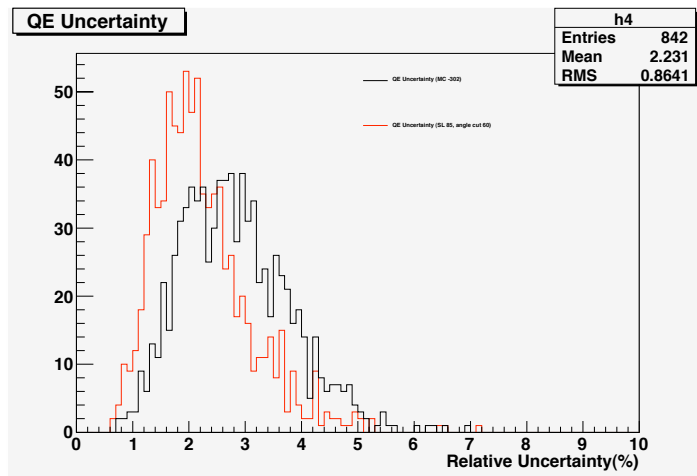
Figure 5.2: Error of QE measurement with old simulation and error of QE measurement with longer scattering length (85cm) and lower incidence angle cut (60∘)

Unfortunately, the improvement on PMTs located in the inner part of the detector is rather small, which makes its effects difficult to be seen on position resolution, etc . But it did give us an interesting insight into the properties of liquid xenon. As mentioned in Chapter 3, Rayleigh scattering length can be estimated by measuring the shadow effects of alpha wires. Such study is yet to be done with the current LXe detector. If scattering length is confirmed to be close to 85cm rather than 45cm as previously thought, the causal relationship with other properties of liquid xenon, such as absorption length, refractive index, group velocity of scintillation light need to be studied as well.

Acknowledgment

Bibliography

[1] T.Mori et al. Research Proposal to PSI, May 1999

[2] Y.Kuno and Y.Okada, Rev. Mod. Phys. **73**, 151 (2001)

[3] J. Hisano et al., Phys. Lett. **B391** (1997) 341

[4] M.L.Brooks et al., Phys. Rev. Lett. **83**(1999) 1521

[5] S.Mihara et al., MEG Technical Note No. 24 (2004)

[6] K. Ozone, Liquid xenon gamma-ray detector for the new$\mu \to e\gamma$ search experiment (2005)

[7] Y.Hisamatsu, Master thesis (2005)

[8] Y.Uchiyama, Master thesis (2006)

[9] R.Sawada, Doctoral thesis (2009)